HExi: A hybrid-electric STOL air taxi for advanced air mobility

AIAA Graduate Team Aircraft Competition 2021-2022

Team HExi

Politecnico di Milano

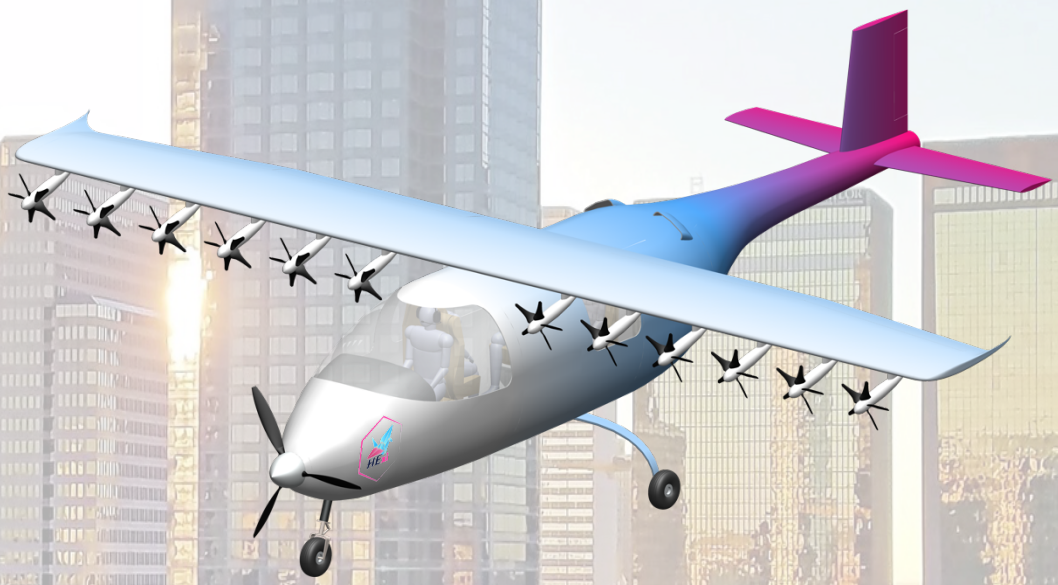

SHAPING THE FUTURE OF AEROSPACE

Team Members

Luca Caccetta
AIAA number 1344826

Maria Ieva
AIAA number 1344729

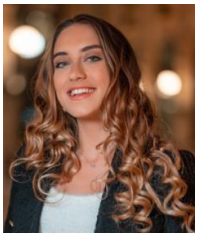

Maria Vittoria Rossetti
AIAA number 1344700

Nicola Tartari
AIAA number 1344705

Matteo Guidotti
AIAA number 1344695

Irene Salmoiraghi
AIAA number 1344701

Anna Sofia Passerelli D'Onofrio
Team Leader
AIAA number 1343781

Team Advisors

Lorenzo Trainelli
Project Advisor

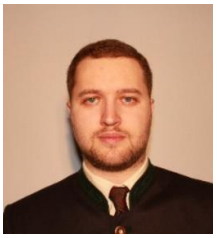

Carlo E.D. Riboldi
Faculty advisor

1 Executive summary

HExi, short for Hybrid Electric Air Taxi, has been designed with the purpose to become the main character of the new green mobility by answering to the RFP of the AIAA Aircraft Design 2021/2022 competition requesting a hybrid electric STOL air taxi.

Among all the requirements, guaranteeing the strict take off and landing distance requirements have been the most critical obstacles to overcome. Therefore, an innovative and changeable propulsion system has been realized. By starting from the emerging DEP system, the blown-wing concept has been implemented to guarantee the demanding aerodynamics imposed by the two critical phases under examination. Moreover, by taking advantage of electric propulsion, during the main part of the flight only a main propeller will be necessary to complete the mission, saving drag and power.

The concept of Urban Air Mobility (UAM) is a sustainable, fast and efficient solution to the problem of conventional means of transport in urban areas. This new approach is supported by more powerful and energy dense batteries and by the continuous development of new technologies. Particularly, during HExi's design process, technologies with a TRL that grants their certified availability within 2026 have been chosen. In this way it's possible to guarantee an entrance in service for 2031 and make HExi competitive in the UAM market that is rapidly expanding.

To conclude, by collecting together innovation, sustainability, cost and maintenance saving, HExi is conceived to become part of the new vision through which the aviation world and air mobility is going to be imagined.

Contents

2 List of symbols and acronyms

Symbol	Definition	Unit
AR	Wing Aspect Ratio	[-]
AR_h	Horizontal Tail Aspect Ratio	[-]
AR_v	Vertical Tail Aspect Ratio	[-]
b	Wing Span	[m]
b_A	Aileron Span	[m]
b_E	Elevator Span	[m]
b_h	Horizontal Tail Span	[m]
b_R	Rudder Span	[m]
b_v	Vertical Tail Span	[m]
C_{AP}	Maintenance Cost	[$]
C_{av}	Avionics Cost	[$]
C_{BAT}	Batteries Cost	[$]
C_{Crew}	Crew Cost	[$]
C_D	3D Drag Coefficient	[-]
C_d	2D Drag Coefficient	[-]
C_{D_0}	Zero-Lift Drag Coefficient	[-]
$C_{D_{0_{cr}}}$	Zero-Lift Drag Coefficient in cruise	[-]
$C_{D_{0_{LND}}}$	Zero-Lift Drag Coefficient during landing	[-]
$C_{D_{0_{TO}}}$	Zero-Lift Drag Coefficient during take off	[-]
C_{DEP}	DEP Cost	[$]
C_{DEV}	Development Support Costs	[$]
C_{EM}	EM Cost	[$]
C_{energy}	Annual Energy Cost	[$]
C_{ENG}	Total Cost of Engineering	[$]
C_f	Flat-plate Skin-Friction Drag Coefficient	[-]
C_{FEES}	Airport and ATM Fees Cost	[$]
C_{FT}	Flight Test Operation Cost	[$]
C_{fuel}	Annual Fuel Cost	[$]
C_{ICE}	ICE Cost	[$]
C_{ins}	Annual Insurance Cost	[$]
C_{insp}	Annual Inspection Cost	[$]
C_L	3D Lift Coefficient	[-]
C_l	2D Lift Coefficient	[-]
C_{L_α}	Lift curve slope	[1/rad]
C_{L_h}	Horizontal Tail Lift Coefficient	[-]
C_{loan}	Annual Loan Payment	[$]
$C_{L_{max}}$	Maximum Lift Coefficient	[-]
$C_{l_{max}}$	Maximum 2D Lift Coefficient	[-]
$C_{L_{max,cr}}$	Maximum Lift Coefficient in cruise	[-]
$C_{L_{max,LND}}$	Maximum Lift Coefficient in landing	[-]
$C_{L_{max,TO}}$	Maximum Lift Coefficient in take off	[-]
C_{L_w}	Wing Lift Coefficient	[-]
C_{MAT}	Material Cost	[$]

Symbol	Definition	Unit
C_{MFG}	Manufacturing Cost	[$]
C_{over}	Engine Overhaul Fund	[$]
C_{QC}	Quality Control Cost	[$]
C_{STOR}	Storage Cost	[$]
C_{Tool}	Tooling Cost	[$]
c_A/MAC	Ailerons Chordwise Location	[-]
c_E/MAC_h	Elevator Chordwise Location	[-]
c_f/MAC	Flap Chordwise Location	[-]
c_R/MAC_v	Rudder Chordwise Location	[-]
$C_{\mathcal{L}}$	Rolling Moment Coefficient	[-]
$C_{\mathcal{L}_\beta}$	Derivative of $C_{\mathcal{L}}$ wrt β	[-]
$C_{\mathcal{M}}$	Pitching Moment Coefficient	[-]
$C_{\mathcal{M}_\alpha}$	Derivative of $C_{\mathcal{M}}$ wrt α	[-]
$C_{\mathcal{N}}$	Yawing Moment Coefficient	[-]
$C_{\mathcal{N}_\beta}$	Derivative of $C_{\mathcal{N}}$ wrt β	[-]
D	Drag	[N]
d_{range}	cruise range	[NM]
E	Young Modulus	[GPa]
e	Stability margin	[-]
e_{clean}	Oswald's factor	[-]
F	Power Index	[-]
F_{exp}	Experience effectiveness adjustment factor	[-]
FF	Component Form Factor	[-]
F_{max}	Maximum power index	[-]
F_{MF}	Maintenance to flight hour ratio	[-]
F_{QDF}	Quantity Discount Factor	[-]
F_s	Stick Force	[N]
G_c	Ratio between linear movement of the stick and deflection of control surface	[-]
G_{max}	Minimum drag to airspeed ratio parameter	[-]
H	Hinge Moment	[Nm]
J	Convex cost function	[-]
k	Induced drag coefficient	[-]
K_{cr}	Induced drag coefficient in cruise	[-]
K_{LND}	Induced drag coefficient in cruise	[-]
k_{NAV}	Navigation Fee Factor	[$/$km$]
K_{TO}	Induced drag coefficient in cruise	
L	Lift	[N]
L_a	Attitude Lift	[N]
L/D	Lift to Drag Ratio	[-]
$(L/D)_{max}$	Maximum Lift to Drag Ratio	[-]
l_h	distance between wing LE and horizontal tail LE	[m]
l_v	distance between wing LE and vertical tail LE	[m]
L_{δ_e}	Control Lift	[N]
M	Mach Number	[-]
M_{bat}	Mass of the batteries	[kg]
M_{EM}	Mass of the EM	[kg]

Symbol	Definition	Unit
M_f	Mass of the fuel	[kg]
M_{PGS}	Mass of the PGS	[kg]
M_{TO}	Mass during take off	[kg]
m/m_{max}	mass components over MTOW	[-]
N	Number of units produced	[-]
n	Load Factor	[-]
N_{break}	Break Even Point	[-]
N_{flight}	number of flight cycles	[flight/year]
N_{hangar}	number of hangar necessary	[-]
$N_{payload}$	number of payload onboard	[-]
P	Power	[kW]
P_a	Available Power	[kW]
p_{hyb}	Degree of hybridization	[-]
P_{EM}	EM Power	[kW]
$P_{EM,n}$	Nominal EM Power	[kW]
P_{ICE}	ICE Power	[kW]
$P_{ICE,n}$	Nominal ICE Power	[kW]
P_r	Required Power	[kW]
P_{rig}	Recuperated power in regeneration mode	[kW]
$P_{Total,n}$	Total Nominal Power	[kW]
Q_{FLGT}	Number of Flight Hours per Year	[-]
Re	Reynolds Number	[-]
S	Wing Surface	[m^2]
S_A	Aileron Surface	[m^2]
S_E	Elevator Surface	[m^2]
S_h	Horizontal Tail Surface	[m^2]
S_R	Rudder Surface	[m^2]
S_v	Vertical Tail Surface	[m^2]
S_{wet_i}	Wet Surface of Component i	[m^2]
T	Thrust	[N]
t/c	Thickness to chord ratio	[-]
V	Velocity	[KTAS]
V_A	Velocity during approach	[m/s]
V_C	Velocity in cruise	[m/s]
V_D	Dive velocity	[m/s]
V_{EAS}	Equivalent Air Speed	[KEAS]
V_F	Flap velocity	[m/s]
V_H	Horizontal Tail Volume Coefficient	[-]
$v_{min,clean}$	Minimum stall speed in clean configuration	[KTAS]
V_s	Stall velocity	[KEAS]
v_{steep}	Steep climb velocity	[KTAS]
V_{TAS}	True Air Speed	[KTAS]
V_V	Vertical Tail Volume Coefficient	[-]
V_v	Vertical speed	[KTAS]
W	Aircraft Weight	[N]
W_{bat}	Weight of batteries	[N]
W_e	Empty weight	[N]

Symbol	Definition	Unit
W_f	Weight of stored hydrocarbon fuel	[N]
W_{ICE}	Weight of the ICE	[N]
W_m	Weight of the electric motor group	[N]
W_{PGS}	Weight of the power generation systems	[N]
W_{pl}	Weight of the payload	[N]
W_{TO}	Weight during take off	[N]
X_{AC_h}	Horizontal Tail Aerodynamic Center	[m]
X_{AC_w}	Wing Aerodynamic Center	[m]
X_C	Control Point	[m]
X_G	Barycenter Position on the X-Axis	[m]
X_N	Neutral Point	[m]
x_s	Stick Linear Mechanical Movement	[m]
α	Angle of Attack	[deg]
α_{cr}	Angle of attack in cruise	[deg]
α_{LND}	Angle of attack during landing	[deg]
$\alpha_{max_{cr}}$	Maximum angle of attack in cruise	[deg]
$\alpha_{max_{LND}}$	Maximum angle of attack in cruise	[deg]
$\alpha_{max_{TO}}$	Maximum angle of attack in take off	[deg]
α_{TO}	Angle of attack during take off	[deg]
β	Sideslip Angle	[deg]
γ	Climb Angle	[deg]
δ_A	Aileron Deflection	[deg]
$\delta_{A,max}$	Maximum Aileron Deflection	[deg]
δ_E	Elevator Deflection	[deg]
$\delta_{E,max}$	Maximum Elevator Deflection	[deg]
δ_f	Flap deflection	[deg]
$\delta_{R,max}$	Maximum Rudder Deflection	[deg]
ε	Borri Stability Parameter	[-]
ε_u	Ultimate Elongation	[-]
ε_α	Derivative of Downwash Angle wrt α	[-]
η_h	Horizontal Tail Efficiency	[-]
η_{cruise}	Main propeller efficiency	[-]
λ	Wing Taper Ratio	[-]
λ_h	Horizontal Tail Taper Ratio	[-]
Λ_m	Sweep Angle	[deg]
λ_v	Vertical Tail Taper Ratio	[-]
ρ	Density	$[kg/m^3]$
σ_b	Tensile Strenght	[GPa]
σ_h	Horizontal Tail Surface Ratio	[-]
ϕ	Bank Angle	[deg]

Acronym	Definition
AC	Aerodynamic Centre
AHP	Analytic Hierarchy Process
AoA	Angle of Attack
ATM	Air Traffic Management
CAS	Calibrated Airspeed
CG	Center of Gravity
CPI	Consumer Price Index
DEP	Distributed Electric Propulsion
EAS	Equivalent Airspeed
ECS	Environmental Control System
EM	Electric Motor
FAR	Federal Aviation Administration
FF	Form Factor
fpm	feet per minute
GA	General Aviation
HS	High Strength
ICAO	International Civil Aviation Organization
ICE	Internal Combustion Engine
IFR	Instrumental Flight Rules
ISA	International Standard Atmosphere
LE	Leading Edge
Li-S	Lithium–Sulfur
LND	Landing
MAC	Wing Mean Aerodynamic Chord
MAC_h	Horizontal MAC
MAC_v	Vertical MAC
MSL	Mean Sea Level
MTOW	Maximum Take Off Weight
NACA	National Advisory Committee for Aeronautics
PGS	Power Generation System
PM	Particulate Matter
PMAD	Power Management And Distribution system
QDF	Quantity Discount Factor
RFP	Request For Proposal
RGF	Reference Geometric Factor
RPM	Revolutions Per Minute
SAR	Specific Air Range
SEP	Specific Excess Power
SMP	Sizing Matrix Plot
STOL	Short Take Off and Landing
SUAM	Sub-Urban Air Mobility
TAS	True Airspeed
TCAS	Traffic Collision Avoidance System
TE	Trailing Edge
TO	Take Off
TRL	Technology Readiness Levels
UAM	Urban Air Mobility
UD	Unidirectional
VTOL	Vertical Take Off and Landing

3 Market analysis

3.1 Introduction

HExi, a hybrid electric STOL air taxi for advanced air mobility, is thought to be a trinomial of Speed, Comfort and Sustainability that'll be the main pillars of the project. The market of air routes is increasingly enlarging and that's why HExi service is thought to be largely distributed all over the USA territory and supported by a mass production. This choice will guarantee a fast spread of the service and a high number of connections. As it'll be explained more in details in the following paragraphs, importance will be also given to affordability and pollution reduction in order to be competitive with already existing taxi services at ground.

3.2 Survey

As a first step, two surveys have been created in order to investigate the situation of public transport in the USA. The first survey has been spread to Italian people in order to understand the needs of tourists or people working abroad (Fig.1a). The second survey has been broaden to American people in order to understand the degree of satisfaction in their public transport and which kind of improvements could be done (Fig.1b).

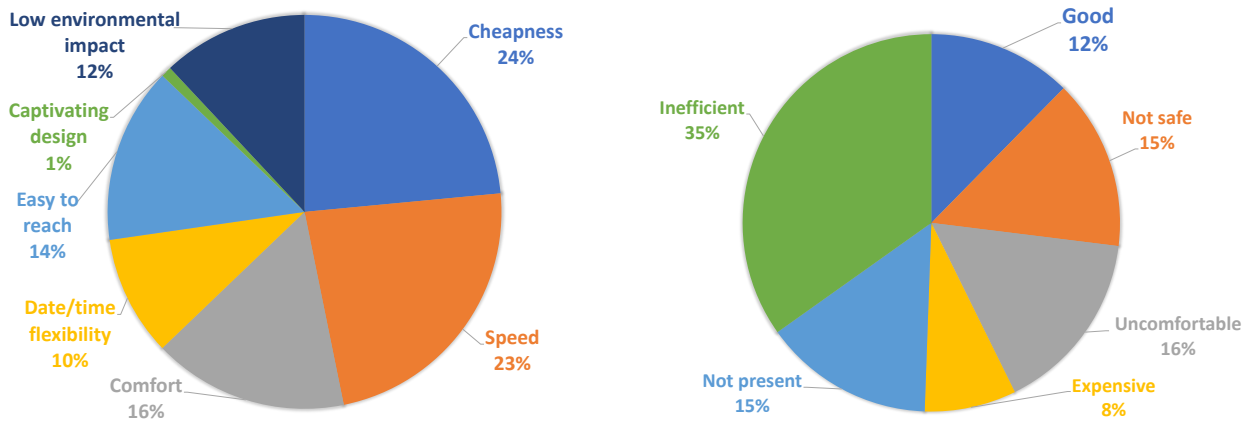

(a) Italian Survey Results.

(b) American Survey Results.

Figure 1: Survey Results.

Combining the results of the two surveys with the objectives previously explained, it has been decided to focus on the states of Texas and California for a preliminary market analysis. The choice of these two states, that show different morphology and weather conditions, opens a wide evaluation field in terms of:

- usability of the service for different purpose (tourism, business trip, etc.);
- HExi's performance (land on different kind of airstrip, fly in various weather conditions)

In conclusion, even if the following market analysis will be focused on two specific states, it'll be possible to guarantee a global service all over the USA territory.

3.3 Main competitors

Short Take-Off and Landing Vehicles (STOL) and Vertical Take-Off and Landing Vehicles (VTOL) are expected to be the dominant players in the urban air mobility and on-demand mobility markets by 2031.

VTOL operations have low ground environmental impact and they are able to maintain minimum overflight requirements. However, the propulsion system of a VTOL vehicle is typically overdimensioned since it is designed for hover requirements. In addition, this oversizing leads to significant noise emissions during take-off and landing as well as cruise range limitations.

STOL aircraft, on the other hand, have less constrained requirements during takeoff and landing phases, so they can have a lighter and smaller propulsion system resulting also in lower noise emissions. For these reasons, STOL vehicles are preferred for Sub-Urban Air Mobility (SUAM) missions with extended range.

3.4 Ground Transportation and Global Pollution Analysis

As shown in Fig.2, buses and cars are the most used means of transport in the USA.

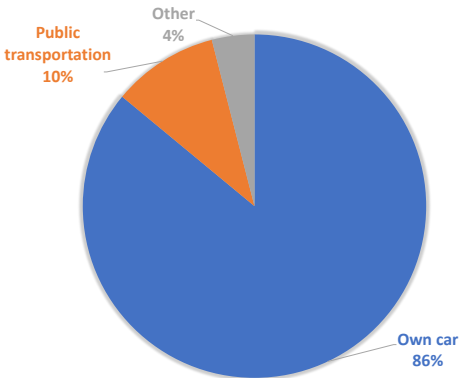

Figure 2: Means of Transport Usage Percentages in the USA.

Consequently, the existing ground transportation infrastructures have been examined for the two selected states in order to investigate the efficiency of connections of the main cities between them and with the outskirts in every State.

The main objective of this analysis is to investigate where to develop the most suitable links to fly with HExi taking also attention to:

- provide the best service in terms of comfort and efficiency (such as faster displacements, no traffic, no delays, no layovers);
- guarantee a lower impact on air pollution

. Particularly, the quality of the air has been evaluated referring to [1] and [2]. California results to be nowadays the least healthy state with a PM2.5 = 13.3. One of the main objectives of *Healthy People 2030* [3] is the reduction of the number of days the population is exposed to unhealthy air. This aim is thought to be pursued by reducing toxic airborne emissions and increasing the use of alternative transportation modes for commuters that is exactly one of the main purposes of HExi.

3.5 Minor Airports Research

As a following step, a thorough research has been conducted in order to identify possible minor airports suitable for previously explained purposes. The main idea, at least for the beginning, is to fly between existing but underused minor airports in order to allow a faster distribution of the service avoiding as well possible delays due to the construction of infrastructures as additional costs. Particularly, in order to create a list of already existing minor airports that could be exploited, the following parameters have been taken into account:

- less than 10 scheduled flight per day;
- at least 300ft length with no material restrictions for runways. This choice, together with following design decisions, will allow to operate both from man-made surfaces and natural surfaces such as dirt and grass runways;
- distant no more than 15 miles from big cities center.
  In particular, this choice was made in order to:
  - reduce possible diseases incoming during the path from/to the airports by minimizing the distance with big cities center;
  - minimize the use of buses and cars to the benefit of air quality;
  - give advantages to outskirts/smaller cities so that it'll be possible to benefit of the service without having to cover high useless distances on ground.

In addition to a reduction of travel time, minor airports have been considered trying to reduce as much as possible connecting time and wait times due to boarding procedures. The selected airports located in Texas and California are reported in Fig.3 and Fig.4.
An in-depth weather analysis nearby selected airports has been conducted too in order to investigate the feasibility of all operations. In particular, temperatures, fog and winds have been evaluated in order to choose the most suitable systems (section 9) to make HExi able to operate under different weather conditions.

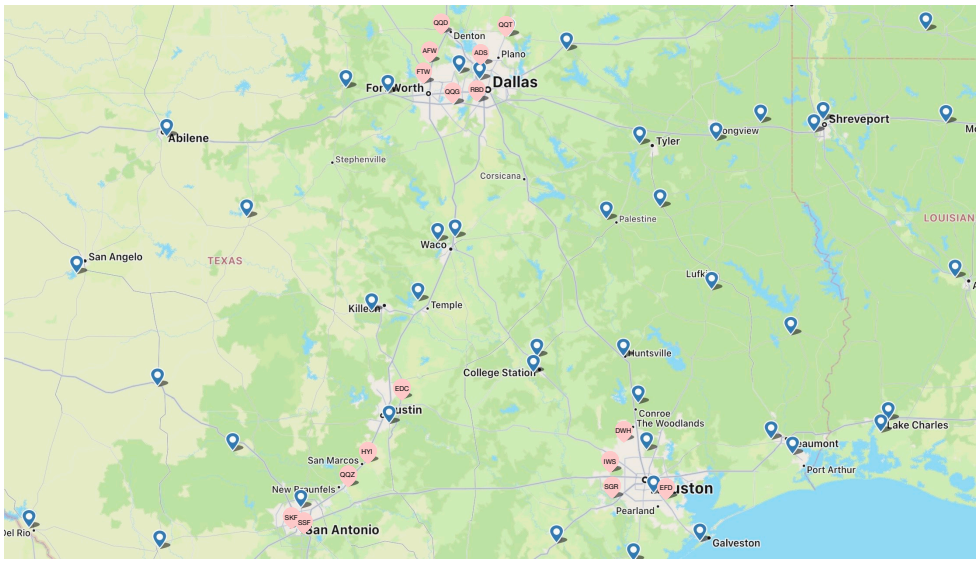

Figure 3: Suitable Minor Airports in Texas - Source: Flightradar24.

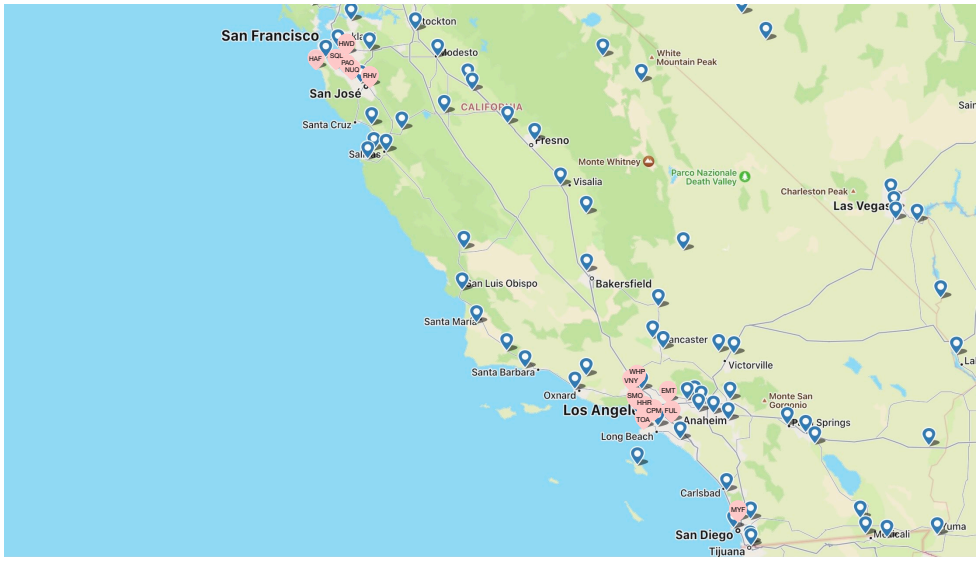

Figure 4: Suitable Minor Airports in California - Source: Flightradar24.

3.6 Candidate Routes Choice

Based on previous considerations, the following two candidate routes have been traced out. As a reminder, these routes are reported only as an example because HExi service is thought to be distributed all over the USA territory. The strategy that has been followed was to provide a link between two big cities far apart (with a maximum of 300 nmi distance) in order to be competitive with higher travel time at ground. Moreover, five intermediate stops are considered to serve outskirts or minor cities badly connected with big ones (with a maximum of 50 nmi distance). For example, in Texas, a possible main route is thought to connect the cities of Houston and Dallas distant about 250 miles with a minimum travel time of 3h 40min by car

and about 4h 40min by bus.

On the other hand, a possible main route in California is thought to be between San Francisco and Los Angeles with a mandatory stop in San Jose, for a total distance of 382 miles and a minimum travel time of 6 hours by car and 9 hours by bus.

3.7 Future Developments

HExi is required to be in service starting from 2031 and, the number of total population is going to grow, as it's possible to note from Fig.5. In parallel, urbanization, traffic and pollution are predicted to increase too.

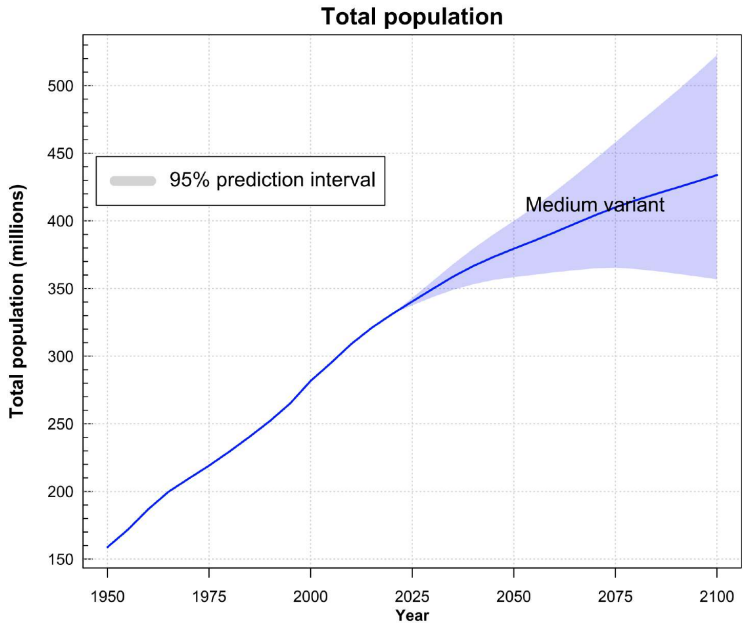

Figure 5: USA Growth Rate - United Nations Department of Economic and Social Affairs Population Dynamics.

In addition to the previous preliminary market analysis where the focus was on the States of Texas and California, general considerations have been done in order to evaluate the feasibility of distributing the service all over the USA territory.

Landing Platforms. The State of New York has been studied as an example and in its region a very few number of suitable minor airports with respect to the other states previously considered has been found. In addition, focusing on New York City, nowadays, it will be easy to still note a high degree of urbanization and efficiency of ground public transport. A good solution in order

to make HExi competitive and able to arrive the nearest possible to high urbanized cities (by reducing travel times at ground) could be the construction of take-off and landing platforms on rivers/lakes.

This solution could be exploited not only for this kind of cities but also in all those areas lacking in airports.

Smartphone Application. HExi service is thought to be distributed mainly by the means of a smartphone application in order to be easily accessible by everyone. Flights will be booked just with a click both with large advance or simply by checking available routes at the time of the booking. Anyway, few physical ticket offices and ticket machines will be set up in order to offer support to the booking process when necessary. Also a phone number for the customer service will be established in order to manage every possible malfunction. Moreover, if necessary, still using the same mobile application, it will be possible to book a complementary taxi service at ground. Conventions with already existing taxi companies are thought to be established in order to guarantee a complete and low cost service. Particularly, companies using electric cars will be chosen in order to ensure lower polluting emissions.

4 Preliminary studies

4.1 Initial configurations

The following configurations have been taken into account during preliminary studies:

Single or twin engine with full electric landing gear: as it will be explained in [4], having a full electric landing gear allows to take off and landing in a shorter runway, without requiring a specific and innovative propulsion system. Therefore, as a first choice, in order to guarantee the requirement on the runway length, this configuration was studied. However, after sizing the baseline mission, it has been noticed that the initial climb requirement is more demanding with respect to take off and landing phases. Consequently, this configuration has been abandoned.

DEP: in order to satisfy the highest lift coefficient estimated, a distributed electric propulsion has been considered. Also in this case, its studies reported that it was not the best choice: by developing different simulations in *OpenVSP*, it has been seen that the hypothesized parasite drag coefficient was never satisfied. Therefore, the following third configuration was built and studied.

DEP configuration during initial and terminal phases and single or twin engine during cruise: because of the high value of parasite drag resulted from the DEP system, it has been decided to implement this scheme combined with the blown effect only for the initial and terminal phases. Therefore, for the main part of the mission, only one nose-mounted propeller or two bigger propellers on the wing tips have been thought to be used. These latter solutions have been simulated in *OpenVSP* to estimate aerodynamic effects and select the optimal propulsion system. Results will be better explained in section 5.

Serial-hybrid configuration is adopted due to its flexibility and the reduced complexity with respect to the parallel scheme.

4.2 Preliminary data and parameters

4.2.1 Preliminary parameters

In order to define the design region, it has been necessary to determine or suppose preliminary aerodynamic coefficients. First of all, a parabolic drag polar has been assumed, as shown in

Eq.1.

$$C_D = C_{D_0} + \frac{1}{\pi e_{clean} AR} C_L^2 \tag{1}$$

where:

- a guess AR = 6.5 has been primarily assumed by looking at existing STOL aircraft listed in Table 1. After a sensitivity analysis made during the Sizing Matrix Plot building, combined with results from the optimizator, the final AR has been chosen equal to 8;

	MTOM [kg]	**S [m²]**	**b [m]**	**AR**	**W/S [psf]**
CH-801	998	15.5	9.6	5.9	13.17
MAULE M-7-260	1134	15.4	10.0	6.5	15.10
Helio H-395 Super Courier	1361	21.5	11.9	6.6	13.90
Bearhawk	1134	16.7	10.1	6.0	13.00

Table 1: Existing STOL aircraft.

- Oswald's factor was computed based on [5] and its value results $e_{clean} = 0.8$;
- For the parasite drag coefficient, a first guess value has been estimated by following the statistic method presented in [5].

Once the majority of components' dimensions were established, C_{D_0} final value has been verified with the build-up approach explained in [6].
More precisely, this method estimates the subsonic parasite drag of each component of the aircraft using:

- a calculated flat-plate skin-friction drag coefficient, C_f that depends on Reynolds number, Mach number, and skin roughness ;
- a component Form Factor, FF that estimates pressure drag due to viscous separation. It is different for all the components of the aircraft, because it depends on their characteristics and it can be computed as shown in Eq.2;

$$FF = \begin{cases} [1 + \frac{0.6}{(x/c)_m}\frac{t}{c} + 100(\frac{t}{c})^4][1.34M^{0.18}(cos(\Lambda_m))^{0.28}] & \text{for wing, tail, strut and pylon} \\ 0.9 + \frac{5}{f^{1.5}+\frac{f}{400}} & \text{for fuselage and smooth canopy} \\ 1 + (0.35/f) & \text{for nacelle and smooth external store} \end{cases} \tag{2}$$

- a factor "Q" that estimates the interference effects on the component drag

The total component drag is finally determined as reported in Eq.3.

$$C_{D_0} = \sum_{i=1}^{n} C_{f_i} FF_i Q_i \frac{S_{wet_i}}{S} + \Delta C_{D_0} \tag{3}$$

where, $f = \frac{l}{\sqrt{(4/\pi)A_{max}}}$.

The term ΔC_{D_0} accounts for additive drag, induced by non-smooth components sticking out into the flow. These contributions are expressed making use of related empirical coefficient C_{D_π}. The latter has been assumed for each additive drag by following the existing values defined in [6] and the sum of all contributes resulted equal to $\Delta C_{D_0} = 0.001$.

Moreover, an increment of 5% with respect to the C_{D_0} value obtain has been considered, in order to take into account the presence of leakage and protuberance, e.g. the cooling contribution. Results are presented n Table 2 for contributions of all components.

Component	**Parasite drag**
Wing	0.0105
Vertical tail	9.2357E-04
Horizontal tail	0.0016
Fuselage	0.0055
Nacelle	3.6572E-05
Leakage and protuberance	9.5090E-04
Total	0.0200

Table 2: Parasite drag components.

It is necessary to underline that the final value is also due to the wing tip contribution: this component allows to decrease both the parasite and the induced[1] drag coefficient. Drag reduction due to the wing tip is reported in Table 3.

	No wing-tip	**Wing-tip**
C_{D_0}	0.0204	0.0200
C_{D_i}	0.0110	0.0108

Table 3: Drag reduction due to the wing tip.

[1]Note that values related to the induced drag coefficients came from the aerodynamic analysis investigated on the final configuration of the aircraft and based on the real polar curve, by following [5]

As a first hypothesis, in order to determine the increment values in TO and LND phases, given range of values in [5] have been considered. However, these phases are characterized by the DEP technology together with the blown-effect. Therefore, several simulations on *OpenVSP* have been developed in order to establish the right drag contribution given by the technologies involved. Particularly, analysis have been implemented with a different number of propellers in order to meet the worst case, since the exact one wasn't still determined. After that, a sensitivity analysis has been executed and the parameters reported in Table 4 reflect the quantities considered for the following design steps.

Configuration	$\mathbf{C_{D_0}}$	$\mathbf{e_{clean}}$	**k**
Clean	0.0200	0.8	0.0474
TO	0.0850	0.78	0.0510
LND	0.1050	0.72	0.0553
Landing gear	0.0028	-	-

Table 4: $C_D parameters$.

In terms of lift coefficients, for the clean configuration a value of $C_{Lmax} = 1.7$ has been assumed, based on typical values reported in [5]. On the other hand, for TO and LND phases, the selection of maximum lift coefficients derived from a sensitivity - first - and then from an optimal analysis, starting from high guess values of respectively 3.5 and 5. Through the latter studies, together with an investigation on the stall velocity, a combination of $C_{L_{max,TO}} = 4$, $C_{L_{max,LND}} = 5.9$ and $v_s = 28$ KEAS resulted as the optimal solution.

It's important to note that the high values reached are needed in order to meet STOL requirements, especially in terms of TO, LND and initial climb.

The increment of lift coefficient has been computed as explained in [7], by starting from a traditional wing with simple high-lift devices.

4.2.2 Sizing Matrix Plot

By taking advantage of the method presented in [5] and flight mechanics equations, the Sizing Matrix Plot shown in Fig.6 figured out. In particular, the requirements that have been taken into account are listed in Table 5 and they are divided in terms of phase and source of derivation: AIAA RFP, certification rules in FAA 14 CFR Part 23 and Team decisions.

Constraint	Condition	Requirement	Requested by
Take-off distance	TO	300 ft @ 5,000 ft	AIAA RFP
Stall speed	LND	28 kts	Team
Initial Rate of climb	Cruise	1500 fpm @ 0 ft	AIAA RFP
Rate of climb	Cruise	750 fpm @ 1,500 ft	Team
Climb gradient	Cruise	8.3% @ 0 ft	FAR 23
Climb gradient - OEI	Cruise	1.5% @ 5,000 ft	FAR 23
Climb gradient- Balked landing	LND	3.3% @ 0 ft	FAR 23
Target cruise speed	Cruise	170 kts @ 10,000 ft	AIAA RFP
Service ceiling	Cruise	100 fpm @ 15,000 ft	AIAA RFP
Instantaneous turn	Cruise	n = 2 @ 100 kts	Team
Landing distance	LND	300 ft @ 5,000 ft	AIAA RFP

Table 5: Requirements for Sizing Matrix Plot.

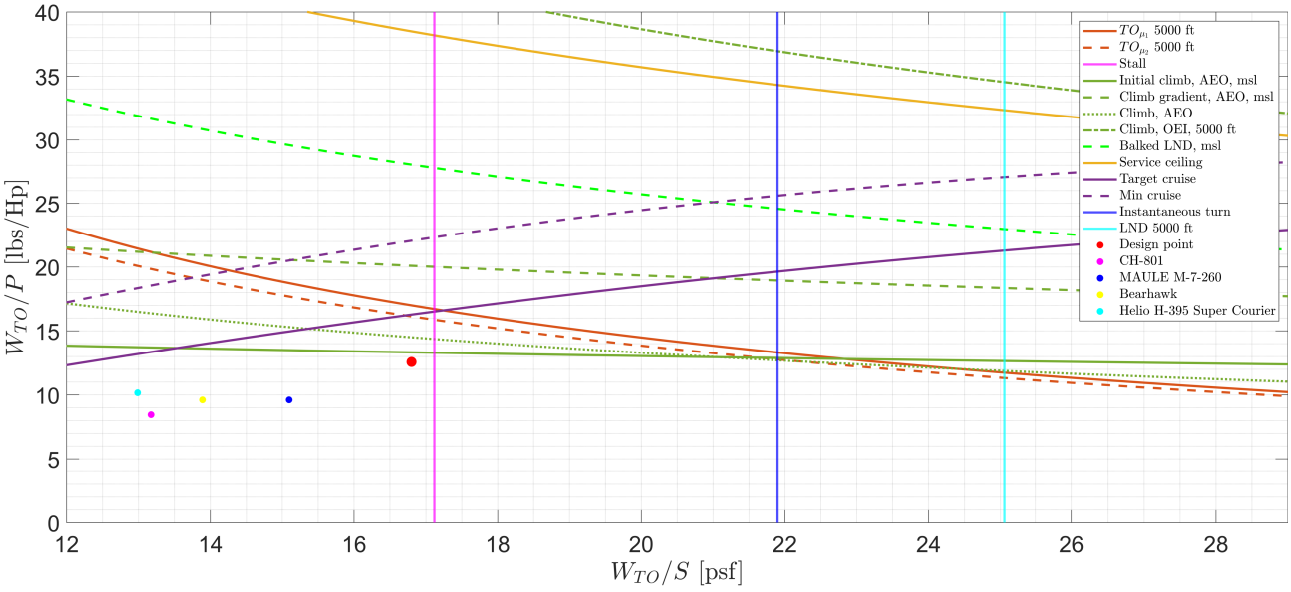

Figure 6: Sizing Matrix Plot.

As expected, the most constrained phases are take-off at 5000 ft, stall and initial climb. These three segments of the mission determine the design region, in which both the optimal design point, $W_{TO}/S = 17.1$ psf and $W_{TO}/P = 10.3$ lbs/Hp, and the existing STOL aircraft taken into account are highlighted. It is noticeable that, on one hand, by fixing the surface, the estimated design point allows the aircraft to fly with a heavier mass. On the other hand, given a certain mass, the airplane under analysis can operate with a lower power.

4.3 Empty mass regression

In order to estimate the empty mass, a logarithmic regression is made in the form proposed by [5], in which the empty mass of existing aircraft is considered deprived of the engine mass. By taking into account 4-seater aircraft built after 2000, the regression is shown in Fig. 7.

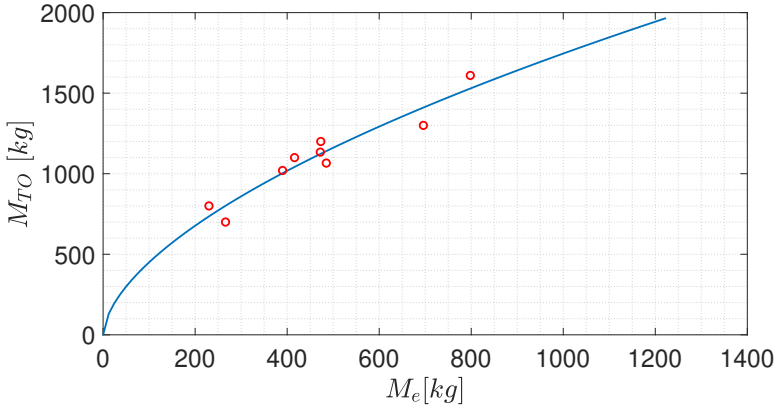

Figure 7: Empty mass vs. Maximum Take-Off mass

4.4 Electric Motor and Generator

A statistical analysis on existing electric motors has been performed, obtaining a specific power of 2.9 kW/kg, far from the demanded power density levels for future hybrid-electric aircraft. In order to take into account the technological developments of electric motors and generators, a specific power of 10 kW/kg has been assumed for 2026 in accordance to [8].

4.5 Internal Combustion Engine

Internal Combustion Engine is used to extend the range and recharge the batteries during cruise. Gasoline engines have been selected because they are quieter, lighter and considerably less expensive than diesel engines of the same power rating. In addition they emit lower CO_2 levels than diesel engines.

A regression relating mass and power rating of existing engines is shown in Fig. 8. Since the ICE needs to be coupled with a generator, the predicted generator power density of 10 kW/kg has been added to the regression.

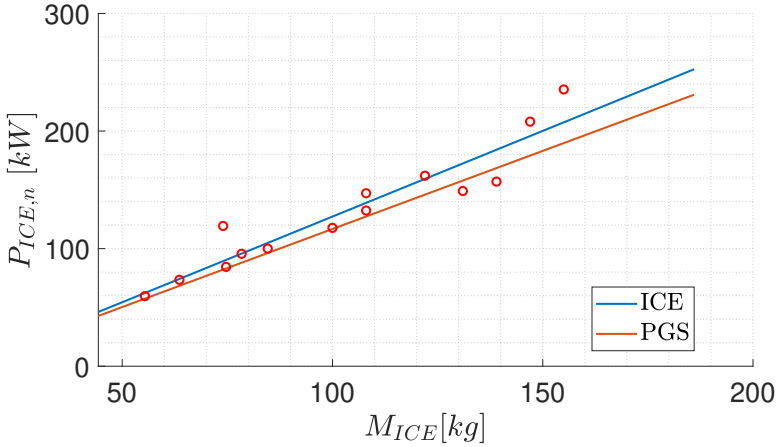

Figure 8: ICE engine and PGS regression.

4.6 Batteries

Batteries represent one of the limiting factors in the development of electric and hybrid-electric aircraft. Specific energy of aeronautical fuel (12,000 Wh/kg [9]) is much higher than last generation Li-ion batteries (100-265 Wh/kg [10]). This makes conventional Li-ion batteries unable to satisfy the demand for new generation of air vehicles.

For this reason, innovative technologies, and new chemistries are considered for HExi design. The choice for the most appropriate one is based on energy density, specific energy, specific power, cycle life, cost and safety. Among all the new chemistries, the most promising ones are Li-S, Silicon anode and Li-metal batteries, that are compared in Fig. 9.

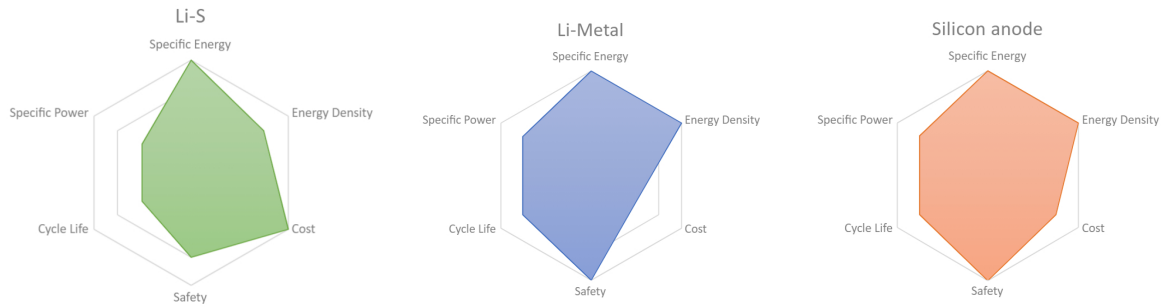

(a) (b) (c)

Figure 9: Batteries features diagrams.

a) Li-metal anodes are being tested by several companies like Quantumscape, Solid Power and Samsung. Specific energies and energy densities are very competitive: they potentially reach values of 900–1900 Wh/L and 400–1000 Wh/kg, as explained in [11].

b) Li-S are appetible due to their high theoretical specific capacity, low cost and nontoxicity. However there are still some challenges impeding the Li–S battery from practical application, such as the shuttle effect. Despite optimal performance reported in several academic papers, the charge/discharge rate can hardly exceed 0.2 C, and the cycle life is no more than 300 cycles [12].

c) Silicon anodes offer more stability than lithium and have an energy density which is 10 times greater than the graphite anodes, most often used in today's commercial lithium-ion batteries, but they suffer from real-world performance issues due to the liquid electrolyte interface stability [13].

Solid-state batteries with silicon anode and NMC 811 nickel rich cathode are the technology chosen by the team. Solid-state electrolyte makes the separation between the anode and cathode more reliable, preventing short circuits, even in the event of misuse or deterioration, therefore the intrinsic safety of the cells increases. Thanks to the solid electrolyte and silicon anode, this technology is lighter, smaller and faster to charge with respect to Li-ion batteries. While solid-state electrolytes themselves may be more expensive than liquid electrolytes, they may enable lower-cost materials and reduce system costs by reducing safety and controls equipment. Following an 8% yearly increase [14], the specific energy at cell level in 2026 is assumed to be 437 kW/kg, as it can be seen in Fig. 10.

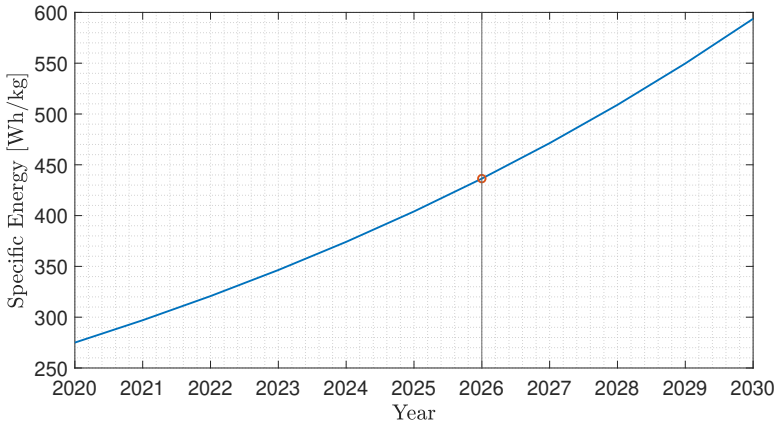

Figure 10: Specific energy projections.

System Packing Efficiency is 80 % and takes into account the weight increasing due to charge-regulator assemblies, heat-dissipation elements, enclosures hardware, cooling, and pack management. Specific power is equal to 3000 Wh/kg and Energy density is 1000 Wh/L. Finally, he number of cycles is 1000 and the projected cost is 100$/kWh.

4.7 Weight Estimation

An optimal approach, like the one proposed by [15], has been adopted to find a design point minimizing the MTOW. This methodology is based on flight mechanics models for calculating the performance parameters of the mission. A set of constraints has been used to meet the requirements coming from RFP, mission analyses and certification barriers.
Take off weight for hybrid-electric aircraft in a preliminary analyses can be split into six principal components, as shown in Eq.4:

$$W_{TO} = W_{PGS} + W_f + W_m + W_{bat} + W_e + W_{pl} \tag{4}$$

where W_{PGS} is the weight of the power generation systems, W_f the weight of stored hydrocarbon fuel, W_m the weight of the electric motor group, W_{bat} the weight of batteries, W_e the empty weight and W_{pl} that of payload.
The sizing mission, described in Table 6, consists of a 300 nmi flight between departure and destination airports, extended considering 20 minutes cruise flight to an alternate aiport and 45 minutes level flight as required for IFR missions. Payload is composed of 4 people, that are the pilot, 3 passengers (for a mass of 345 kg) and 40 kg of baggage and battery are charged during

cruise phases.

Phase	Altitude	Airspeed	Propulsion	Requested by	Notes
Taxi	0	-	Electric	Team	5% battery energy
Take-off	0 ft	-	Electric	AIAA RFP	Grass
Initial climb	0-1,500 ft	65.0 KTAS	Hybrid	AIAA RFP	V_V=1500 fpm
Climb	1,500-10,000 ft	75.3 KTAS	Electric	Team	V_V=750 fpm
Cruise	10,000 ft	170 KTAS	Hybrid	AIAA RFP	-
Descent	10,000-5,000 ft	100 KTAS	Electric	Team	-
Flight to alternate airport	5000 ft	120 KTAS	Electric	FAR 23	20 min
Level flight	5,000 ft	150 KTAS	Hybrid	FAR 23	45 min
Descent	5,000-0 ft	100 KTAS	Electric	Team	V_V=500 fpm
Landing	0 ft	-	Electric	AIAA RFP	Grass

Table 6: Sizing mission.

The convex cost function in Eq. (5) is composed of the sum of the square weights normalized with respect to a constant reference factor.

$$J = \left(\frac{W_{ICE}}{W_{ICE,ref}}\right)^2 + \left(\frac{W_f}{W_{f,ref}}\right)^2 + \left(\frac{W_m}{W_{m,ref}}\right)^2 + \left(\frac{W_{bat}}{W_{bat,ref}}\right)^2 \tag{5}$$

The constraints imposed for the design mission are:

- takeoff and landing distance must be less than 300 ft, considering an obstacle 50 ft high both on grass and asphalt surfaces and also at 5000 ft +18°F;
- battery power must be limited in a range between 15% and 95% of the maximum battery capacity;
- W_{TO} must be within the range of ± 5% with respect to the regression proposed in Fig. 7; This value takes into account a reasonable uncertainty margin when looking at the aircraft considered.
- the flight must be completed with at least 5% of fuel reserve;
- an upper limit to the (W_{TO}/P) ratio has been set based on the Sizing Matrix Plot requirements while (W_{TO}/S) is fixed.

4.8 Sensitivity analysis and final results

Sensitivity analysis has been conducted varying aerodynamics coefficients, battery parameters and initial conditions:

- the method is robust with respect to a variation of initial conditions;
- a 10% increase of $C_{D_{0_{LND}}}$,K_{LND},$C_{D_{0_{TO}}}$ and K_{TO}, determine a marginal variation of the final Take-Off weight (less than 1%);
- Take-Off weight is heavily influenced by $C_{D_{0_{LND}}}$.
- a 10% variation of battery specific energy leads to a 10% variation of the final Take-Off weight.

Final results are presented in Table 7.

Parameter	**Value**
M_{TO}	1210.9 kg
M_{PGS}	133.5 kg
M_f	88.2 kg
M_{EM}	21.5 kg
M_{bat}	87.7 kg
S	14.8 m^2
P_{ICE}	162 kW
P_{EM}	215 kW
W_{TO}/S	805 N/m^2
W_{TO}/P	0.055 N/W

Table 7: Optimizer results.

5 Configuration

As anticipated in section 4.1, in terms of the propulsion system, the third configuration has been carried on in order to reach the high lift coefficient values estimated during the preliminary design. Therefore, a DEP scheme together with the blown effect has been developed, because none of the most complex conventional high-lift devices allow to reach the desired aerodynamic quantities.

More precisely, for the DEP contribution, twelve small propellers in front and under the LE of the wing have been designed. As explained in the preliminary studies, flying all the mission with only this propulsion configuration doesn't guarantee the parasite drag coefficient estimated in clean configuration. Consequently, a changeable scheme during the flight has been developed: as a first choice, two bigger propellers on the wing tips were considered for covering the main part of the mission. However, in terms of both aerodynamic effects and manufacturer complexity, a single nose-mounted propeller might be simpler. Therefore, several simulations and studies through *OpenVSP* tool have been carried out to determine a comparison between the two cases presented.
It ended up that a single engine on the nose allows to conduct the flight guaranteeing the thrust and aerodynamics required by the mission. These results determined the final configuration that is going to be presented: a single engine on the nose for the main part of the mission and the folding DEP system improved with the blown effect for the TO and LND phases.

By focusing on the wing vertical position, based on the design requirements, a trade-off among all the characteristics of low-, medium- and high-mounted wing has been developed. As explained in [16], the last configuration is not really suggested for STOL aircraft, due to its lower lift capabilities with respect to the other choices. However, as stated in the requirements, HExi must be capable to take off and land in different types of runways. Therefore, due to this constraint, together with the DEP system position under the leading edge of the wing and other less significant characteristics, a high-mounted wing was chosen. Note that, despite of the lower lift capabilities of a high wing configuration, the unconventional propulsion system allows to

overcome this problem and guarantees reaching the estimated aerodynamics values, as will be better explained in section 7.2.1.

As for the position of the vertical and horizontal tail, by considering different characteristics and studying the interaction with the wing, it resulted that a conventional tail can meet all the requirements. Moreover, this choice has been confirmed from the aerodynamics simulations made with both *xflr5* and *OpenVSP* tools.

Finally, because of the cruise speed values that have to be guaranteed and the low parasite drag, a retractable landing gear has been selected and designed, as will be deeper treated in section 8.2.

6 Propulsion system

6.1 Battery Sizing

The battery packs, having a total capacity of 30.7 kWh, have been sized considering also the additional volume requirements caused by the necessity to have a cooling system [17].
As a first approximation for the latter system it has been assumed to use a fluid with an average density equal to 970 kg/m^3 and specific heat capacity coefficient of 3.7 kJ/kgK.
The battery system is divided in 3 pack different sized for optimize the space inside the aircraft as much as possible. The minimum unit of the battery system is the cell, whose dimensions are 11 cm x 11 cm x 0.25 cm. Between each cell a series of appropriately sized tubes containing the cooling liquid is present, as shown in Fig. 11. This allows the battery cells to operate around the optimal temperature of 20 °C. The weight breakdown is presented in table Table 8.

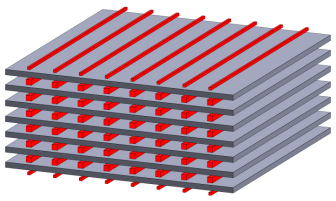

Figure 11: A module of Battery System: in red cooling system, in grey cells.

Compontent	**Weight**
Battery	73 kg
Liquid Cooling	6 kg
System	6 kg

Table 8: Battery system weight breakdown.

Solid state batteries are able to charge from 20% to 90% in approximately 15 minutes, thus enabling fast charging between two consecutive flights. This can be done through a plug-in charger on ground. Battery can also be charged during cruise phases exploiting the PGS and during descent flight by using the main propeller in recuperation mode.

6.2 Power Generation System

Thermal engine design point is very close to UL520T Fig. 12, a turbocharged, 6-cylinder with multipoint ingestion. It is capable of nominal 162 kW power at 2700 RPM up to 15,000 ft. The declaired TBO is 1000 Hr and a price of 48,000 USD as confirmed by the manufacturer. In Table 9 the performance of the ICE are reported.

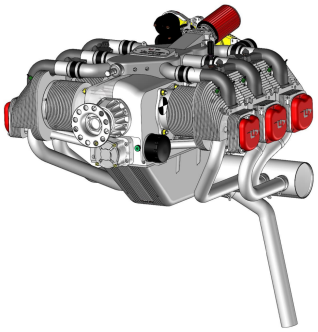

Figure 12: UL520T side view.

Parameter	Value
Weights	120 kg
Max Torque (ISA condition)	585 Nm @ 2,300 RPM
Power rating (ISA condition)	162 kW @ 2,700 RPM
Fuel	MOGAS with min. 97 octane rating or AVGAS (100LL or UL91)

Table 9: UL520T Data.

UL520T requires oil and air cooling, as specified by the technical manual [18]. In particular air system need an entrance surface ranging from 70 to 100 cm^2, positioned on the back of the aircraft. While the exhaust pipe it is place under the tailcone.

Finally, aviation gasoline (Avgas) is the selected fuel and it is the most commonly used in piston-engine aircraft. For this reason it is easier to be found also in smaller airports. This leaded fuel contains Tetra-Ethyl-Lead (TEL), which is an additive used to prevent engine damage at higher power settings.

ICE needs to be coupled with a generator that converts mechanical power to electrical power, necessary to recharge the battery and power the main EM. A custom generator is used, with and efficiency of 98%, weight of 15 kg and a power density of 10 kW/kg.

6.3 EM for main propeller

From the sizing mission analysis, the electric motor should provide a continuous power of 150 kW during climb and 133 kW during cruise phase.

The selected motor (Fig. 13) is the HPDM-250 by H3X [19], an integrated motor drive suitable for aerospace applications having an ultra-high specific power of 12 kW/kg including the gearbox.

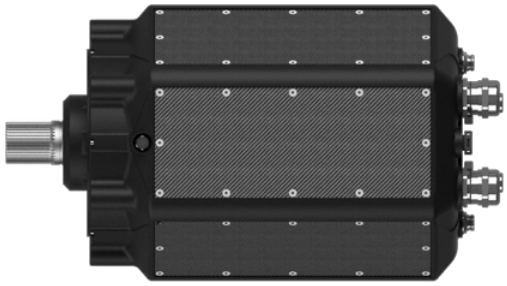

Figure 13: HPDM-250 side view.

Currently under testing phase, its specifications are shown in Table 10.

Parameter	**Value**
Continuous Power	200 kW
Peak Power	250 kW
Peak Duration	30 s
Speed range	0 - 20,000 RPM
Dry mass	13 kg
Efficiency in cruise	91%

Table 10: HPDM-250 Data, direct drive

Being a brushless motor it is more powerful, lighter, more efficient and needs less maintenance than a brushed one. It is coupled with a 5:1 gearbox weighting 4 kg and having an efficiency of 98%.

During cruise flight the motor-gearbox unit provides the propeller with a torque of 460 Nm at a speed of 2200 RPM and has a total efficiency of about 90% as measured during experimental tests carried out by the manufacturer.

As reported by H3X, this motor can also be used as a generator as it is capable of four-quadrant operation. This mode can be exploited during descent flight if the propeller is used as an

airborne wind turbine. In this case the potential energy of the descending aircraft is converted in electric energy and stored in the battery.

6.4 Main Propeller

6.4.1 Design of the baseline propeller

From an analysis on the propellers used in similar aircraft, an initial diameter of 1.90 m has been selected. Then a trade-off study has been made considering the following criterias:

- Mach number at blades tip should not exceed 0.75 in order to avoid transonic effects;
- there must be enough clearence between the propeller and the nose gear;

After few iterations the final propeller diameter is assumed to be 1.75 m with an hub diameter of 0.35 m. The selected airfoil is the CLARK Y, typically used in aeronautical applications.
A preliminary sizing has been made using the software *JavaProp* and evaluating the design parameters at cruise conditions. Rotational speed of the propeller is set to 2200 RPM looking at the EM operating point and considering the 5:1 reduction factor due to the gearbox. Performance of the baseline propeller are shown in Table 11.

Parameter	**Value**
Blades	3
Diameter	1.75 m
Cruise RPM	2200
Cruise Efficiency	90%

Table 11: Baseline propeller performance.

6.4.2 Recuperation mode

One of the advantages of serial hybrid-electric propulsion is being able to take advantage of regeneration. In this phase the propeller behaves like an airborne wind turbine and develops negative thrust, while conveying mechanical power to the shaft. The energy recuperation mode can be exploited in the descent phase, where the energy required is very low, in order to recover electrical energy that will be used to recharge the batteries.

Regeneration performance of the baseline propeller are evaluated at an altitude of 5,000 ft and an airspeed of 100 KTAS as imposed in the sizing mission. During this phase the recovered power is 3400 kW.

6.4.3 Propeller optimization

Baseline's propeller geometry is then optimized in order to maximize simultaneously the cruise efficiency and the power recovered in the descent phase. The optimization algorithm used is interior-point and the cost function is:

$$J = -\left(\sqrt{\eta_{cruise}{}^2} + \frac{\sqrt{P_{rig}{}^2}}{P_{rig,ref}} \right) \tag{6}$$

Where P_{rig} is the recuperated power in regeneration mode and $P_{rig,ref}$ is a fixed reference value chosen arbitrarily. A minus is placed because *fmincon* searches the minimum of the cost function and the square root of the second power is adopted to make sure that the function is always negative [20].

The optimization process is subject to several constraints taking into account geometrical limitations of chord and twist angle distributions.

Final parameters are reported in Table 12 and the blade is shown in Fig. 14.

Parameter	**Value**
Blades	3
Diameter	1.75 m
Cruise RPM	2200
Cruise Efficiency	85%
Recuperated Power	6248 kW
Blades Material	Aluminium
Total mass	5 kg

Table 12: Baseline propeller performance.

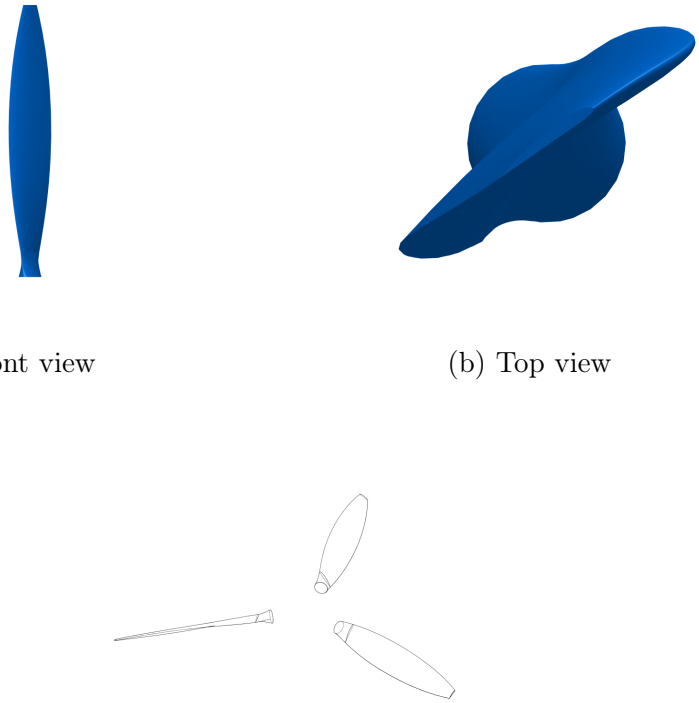

(a) Front view

(b) Top view

(c) 3D view

Figure 14: Main propeller.

Recuperated energy during a full descent from 10,000 ft to MSL is 2041 Wh, which corresponds to about the 6.7% of full battery capacity.

Therefore, this technology enables to reduce the embarked fuel or the time to fully recharge the batteries on the ground. In addition, such a system enables recharge with the aircraft parked on the field facing upwind.

6.5 DEP Sizing

The purpose of the DEP system is to increase the lift coefficient during terminal phases. An initial geometry has been designed following the approach presented by [7], resulting in an array of twelve propellers distributed along the wing's leading edge with a diameter of 0.6 m. Maximum lift coefficient value of 6 is reached in stall conditions, as shown in Fig. 15.

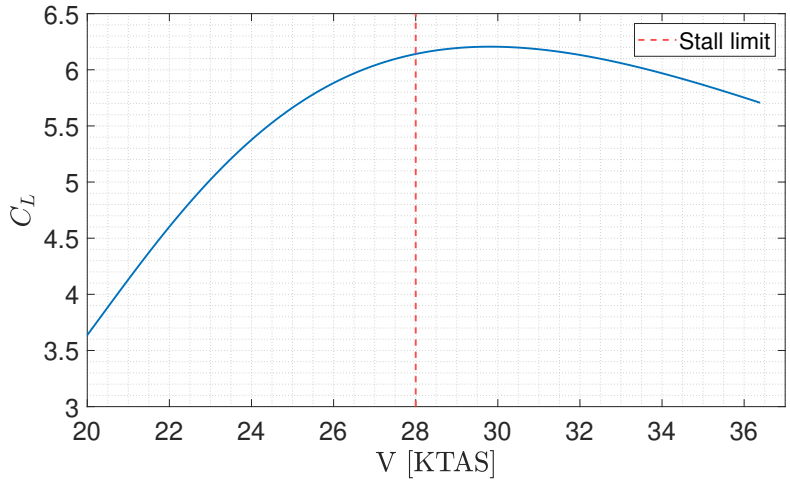

Figure 15: Blown wing lift coefficient estimation

Required axial induction factor for each propeller at Touch-Down airspeed of $1.1V_s$ is equal to 0.8821. This result is the starting point for DEP's propeller blade design.

6.5.1 Blade design

The high lift propeller design proposed by [21] has been implemented with the goal of providing a near-uniform axial velocity increase aft of the propeller. By using this method, the designed propellers require approximately 15% less power but produce approximately 11% less thrust with respect to the conventional ones, which have a higher degree of non-uniformity in their induced velocity distributions. The method requires as input the axial induction factor computed in section 6.5.

Final parameters are reported in Table 13 and propellers are shown in Fig. 16a.

Parameter	**Value**
Blades	5
Diameter	0.6 m
Touch-Down RPM	5000
Take-Off RPM	5500
Blades Material	carbon fiber and epoxy resin
Total mass	1.25 kg

Table 13: DEP blade properties.

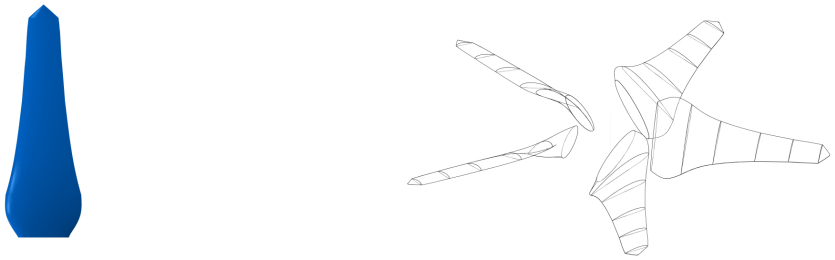

(a) Front view of the DEP blade. (b) DEP blades 3D view.

Figure 16: DEP blades 3D view.

DEP propellers are able to produce a reverse thrust when spinning in the opposite direction. This operational mode is used during landing phase in order to satisfy the short landing requirement.

6.5.2 Folding propeller DEP

Hexi's configuration is based on the use of a single pulling propeller on the nose and a series of small propellers on the wings, which allow to achieve higher values of C_L. Since DEP is only deployed in Take-Off and Landing phases, in order to mitigate the increase of C_{D_0} in cruise, a folding blade system has been devised. The idea is based on the model developed for the NASA X-57 Maxwell [22]. The propellers are presented in Fig. 17 for both folded and unfolded configuration.

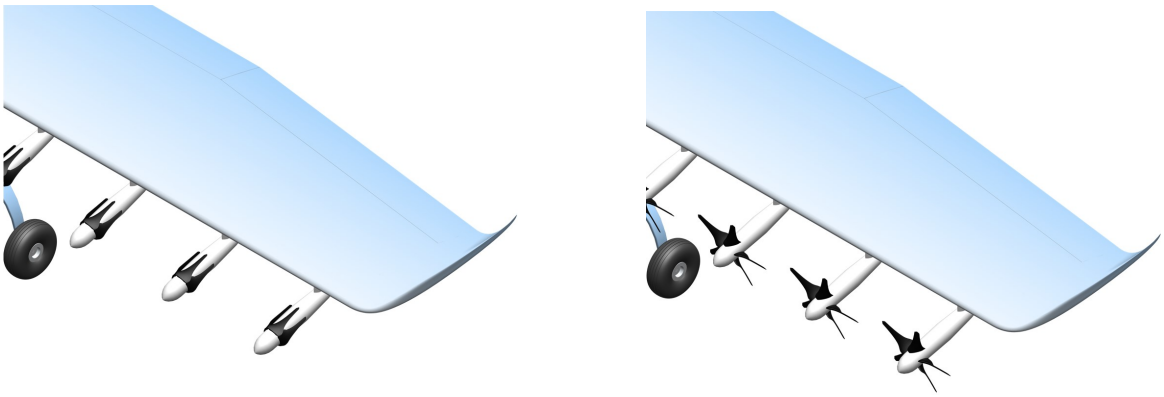

Figure 17: Folded and unfolded propellers configurations.

6.6 EM for DEP

From the design of the DEP propellers, the electric motor should provide a continuous power of 10 kW and a peak of 20 kW. The selected motor is the NEUMOTOR 4420 [23] (Fig. 19), that is a brushless motor with a liquid cooling system integrate. The characteristic are listed in Table 18.

	Direct drive
Weight	3 kg
Max Continuous Power	10 kW
Max Peak Power	20 kW
Max RPM	10000
Weight	3 kg
Diameter	127 mm
Length	102 mm

Figure 18: NEUMOTOR 4420 Data.

Figure 19: NEUMOTOR 4420 view.

6.7 CO_2 emission

To limit the effects of climate change, the United States (Fig. 20) should eliminate most of the carbon emission derived by the transportation sector in the next 20 years, but currently this trend is not met [24].

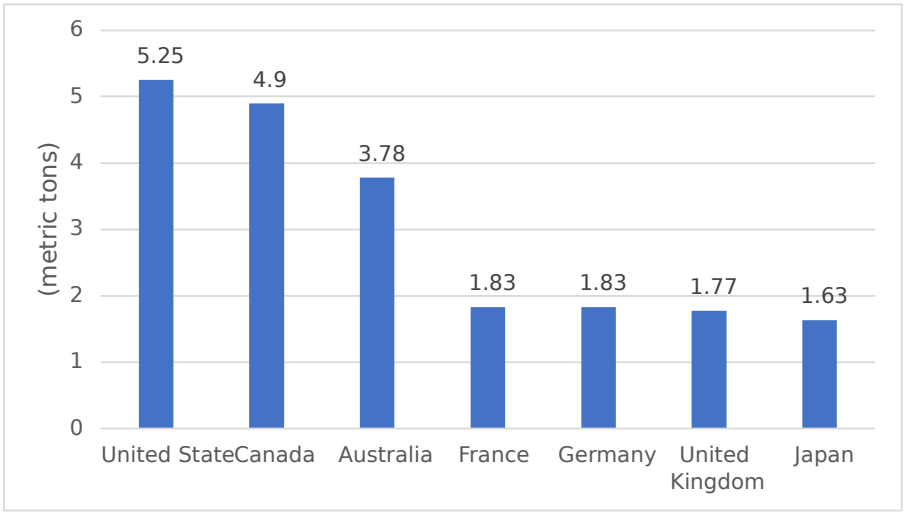

Figure 20: Transportation Carbon Dioxide Emissions per Capital by Country

That's the result of a transportation policy framework that prioritizes cars and highways

development, which has not changed much in the last 60 years, despite the international agreements taken by the US.

The U.S. Public Interest Research Group and the Frontier Group published a new report [25] outlining 50 steps to eliminate carbon pollution from the transportation sector by encouraging low-carbon modes of travel, more efficient development and cleaner vehicles.

The main pollutant emitted is carbon dioxide, CO_2, which is responsible for the greenhouse effect and toxic to the planet and humans. CO_2 is considered a global pollutant and must be reduced at any stage of flight. Taking advantage of the CO_2 estimation methodology described by the EPA, the emission during flight can be estimated as [24]:

$$CO_2 = \frac{\left(\frac{1}{SAR}\right)_{avg}}{RGF^{0.24}} = 34\frac{pass * g}{km} \tag{7}$$

By comparing the average emission in US (Fig. 21), it can be seen that HExi appears to be extremely competitive with current modes of transport. Therefore, the use of this aircraft can significantly contribute to the reduction of CO_2 emissions in the transportation sector. HExi could be a major innovation in U.S. transportation and contributes on a large scale to the abatement of CO_2.

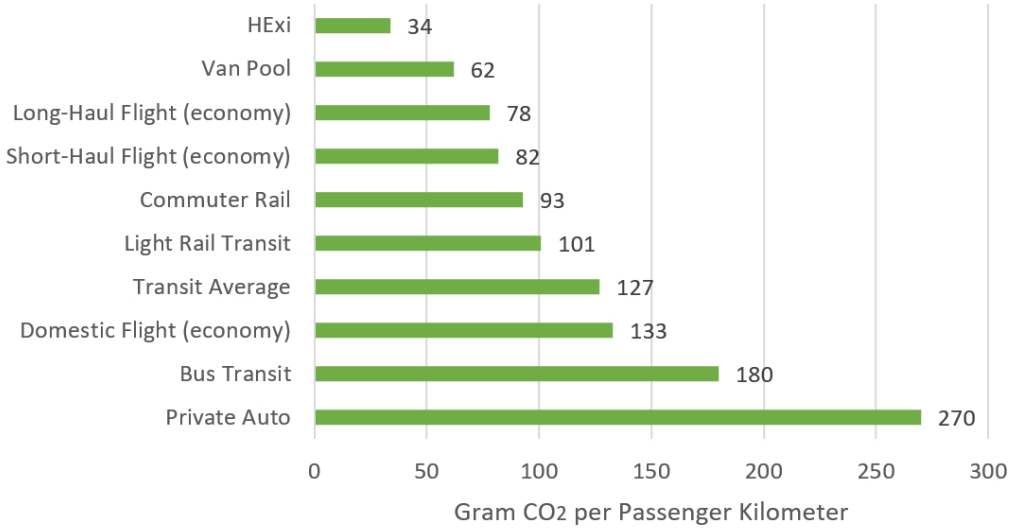

Figure 21: CO2 emission per passenger km of various transportation modes.

7 Aerodynamics

7.1 Wing airfoil selection

In order to select the best airfoil(s), an AHP method has been implemented.
First of all, a list of airfoils to be considered has been created by highlighting different aspects of the airfoils that could be translated into aerodynamics advantages. As a first constraint, the thickness of the airfoil has been taken into account. Only values greater than 12-13% have been accepted by considering the necessity to allocate fuel tanks and other equipment.
An other important feature asked to HExi's wing airfoil is a quite high lift coefficient, due to the significant values estimated in both TO and LND phases. Because of this fact, lots 5-digit NACA airfoils have been considered, given that they guarantee higher lift coefficients, lower drag and moment coefficients with respect to the 4-digits category.
Finally, based on both [26] and [27], the selected airfoils are: NACA 23012, NACA 23015, NACA 23018, NACA 2412, NACA 4412, NACA 4415, NACA 4421, NACA 63212, NACA 63412, NACA 63415, NACA 63615, NACA 63412A, NACA 65415, GAW-2, GAW-2 mod, USA35b.
The constraints taken into account to build the AHP program are listed below:

- $C_{l_{max}}$;
- lift to drag ratio L/D;
- minimum C_{D_0};
- greater stall α;
- pitching moment coefficient;
- drag bucket

The analysis of the airfoil has been implemented through *xflr5* and, by considering the characteristic airspeed of flight, Re = 6E+06 and a M = 0.2 have been taken into account for the simulations.
From the AHP analysis, the two best airfoils are GAW-2 and NACA 4412, whose aerodynamics characteristics are reported in Fig.22a and Fig.22b.

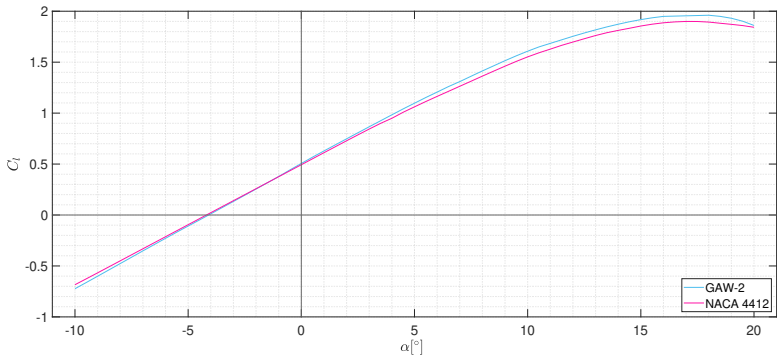

(a) Lift coefficient vs α comparison.

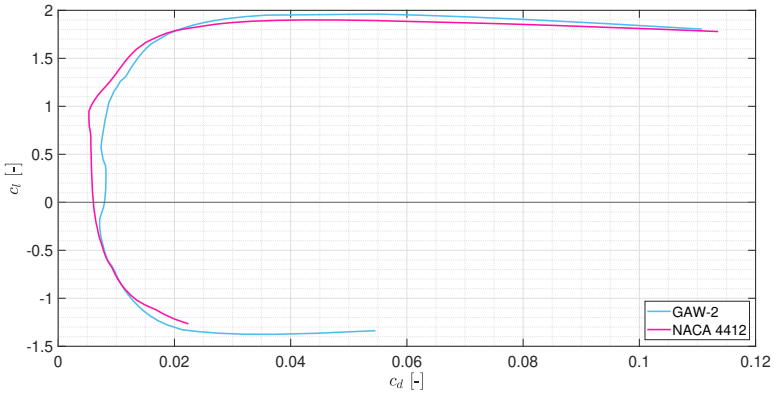

(b) Polar curves comparison.

Figure 22: Polar curve.

Since the obtained results are very close to each other, in order to select the best one for HExi's wing, a sensitivity analysis has been implemented, ending up with the GAW-2.

Note that, due to the affinity of the results between the two selected airfoils, before going on with the design considering only GAW-2, a study on developing a combined wing has been considered. Particularly, it has been assumed to match the two different profiles GAW-2 and NACA 4412 between the root and the tip of the wing. However, this examination didn't lead to significant improvements in terms of aerodynamic advantages, so the single GAW-2 profile configuration has been confirmed. This choice has also been made in order to get simpler manufacturing and reducing production costs. In Fig.23a and Fig.23b lift-VS-AoA and polar graphs of the GAW-2 airfoil are respectively presented, together with the experimental data executed at Re = 1E+06 in [27] [2].

[2]It is clear that the gap between the simulations' Re and the highest one available from experiments is quite different, but a strong affinity can still be visualized.

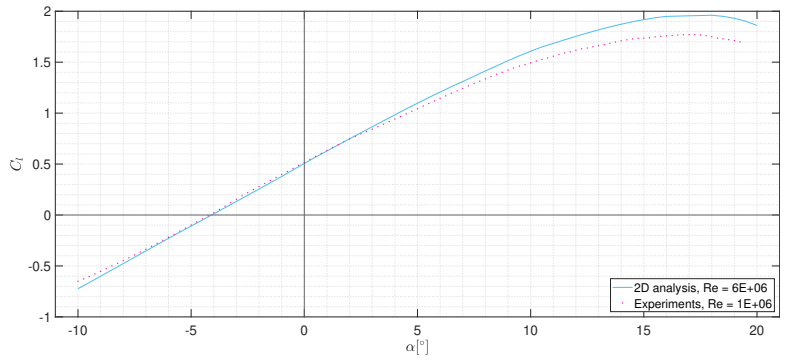

(a) Lift coefficient vs α.

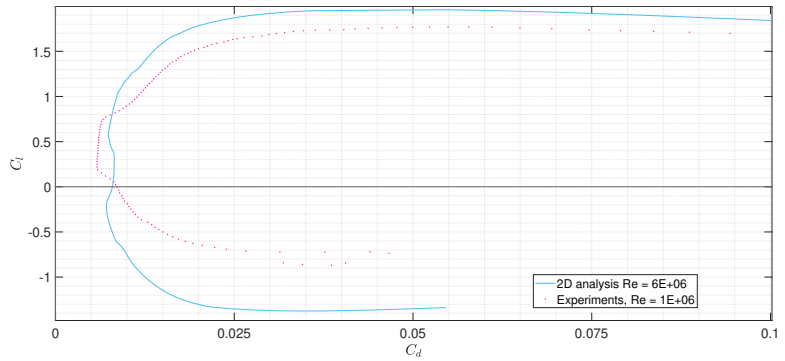

(b) Polar curve

Figure 23: Airfoil aerodynamics data.

7.2 Wing design

First of all, by following [16] and [5], a *MATLAB* code for calculating all the aerodynamics and geometric parameters based on preliminary studies results has been developed. In particular, the target and the maximum lift coefficient have been computed and verified in the main three phases on which the design is based: TO, cruise and LND. The resulting values are presented in Table 14. Note that also the clean wing case is reported because the final wing design will be based on those values in terms of lift capabilities.

Phase	$\mathbf{C_L}$	$\mathbf{C_{L_{max}}}$
TO @ 5,000 ft	3.3	4
Cruise @ 10,000 ft (only wing)	0.24	1.8
Cruise @ 10,000 ft	0.23	1.7
LND @ 5,000 ft	4.87	5.9

Table 14: Target lift coefficients for the sizing phases.

The aim of these calculations was to set all the goal values that had to be verified as well through *xflr5* for the clean wing as through *OpenVSP* for the blown-wing and the entire aircraft. Two

different programs have been used because the second one is more suitable for testing the effects of the blown technology, as it will be better explained in section 7.2.1. On the other hand, in order to verify the meeting of the base aerodynamics characteristics and to set the starting point for the blown-wing integration, *xflr5* allows to study all the significant parameters in terms of coefficients, lift distribution, AoA, drag and moments.

After having set the vertical location (section 5) and all the goals to be satisfied, a sensitivity analysis among all the geometric parameters has been carried out.
The design of the wing has been optimized for the cruise phase after the study on the impact of the distributed electric propulsion, as stated in section 5. In fact, HExi aircraft takes advantage of the DEP system only during the initial and terminal phases of the mission. Of course, because of the constant presence of the propellers along the leading edge of the wing, a geometric constraint on the span had to be considered. Consequently, after an iterative analysis in which both aerodynamics and propulsion effects have been taken into account, the following results have been obtained: a wing span $b = 10.87m$ and an AR $= 8$ confirming preliminary studies.
In terms of shape, the following configurations have been tested: rectangular, full-tapered and semi-tapered wing.
At first, a comparison between the rectangular geometry and taper values of 0.9, 0.8 and 0.7 has been developed. As a result, in order to obtain a trade off among desired lift coefficient, low induced drag and bending moment, the selected taper ratio is $\lambda = 0.8$.
Moreover, it has been studied the effect of a semi-tapered geometry, ending up with a final configuration composed by a rectangular shape up to the 60% of the wing span and $\lambda = 0.8$ until the wing tip.
This choice has been made for a trade-off between the simplification of the design and aerodynamic advantages. An additional analysis has been carried out in terms of angles in order to evaluate their impact on aerodynamics characteristics:

- imposing a dihedral angle didn't led to significant advantages,so it is kept equal to zero for the final design;
- typical values for the twist angle are found to be between $0°$ and $-4°$ from literature ([16], [5], [28]). After multiple analysis, it results that keeping a null twist angle guarantees an

almost elliptic lift distribution along the span for the clean wing (as reported in Fig.24). Consequently, the twist angle is also set to zero for a simpler design choice.

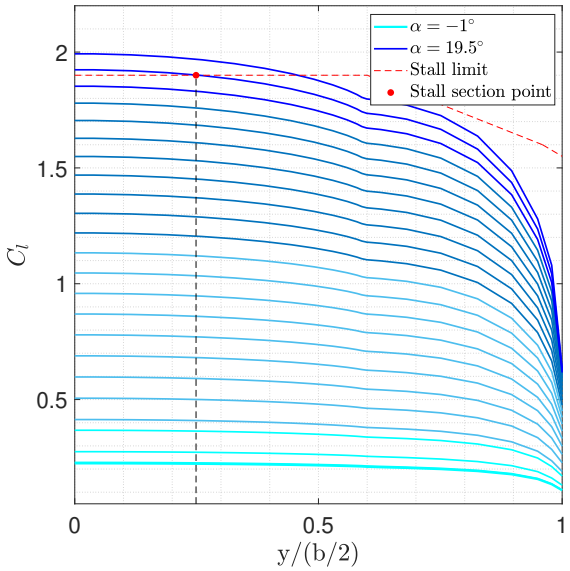

Figure 24: Lift distribution.

Still considering Fig.24, it is possible to note that the stall AoA reached by the selected configuration corresponds to the 25% of the semi-span. Fig.24 is built in *MATLAB* taking advantage of data obtained from *xflr5* analysis, by considering both a *VLM* analysis and a *lift line theory* one. However, the *lift line theory* is only reliable for low values of AoA and so a trade-off between these two methods with a safety margin on the AoA has been considered leading to the final value for the clean stall AoA equal to 19°.

It is necessary to highlight that nearby the tip of the semi-span, the behaviour of lift is not properly as expected. This attitude is due to the impossibility of designing a smoother and more optimal wing-tip in the software *xflr5*. However, the tarnish region is very restricted and, in terms of aerodynamics parameters, it doesn't affect the effective results and the wing design. As previously anticipated, in order to set back the tip flow separation, an upturned booster wingtip has been considered and designed.

The shape of the wingtip has been selected accounting for both the construction simplicity and the good effects on aerodynamics.

In particular, an angle of 40° with respect to the wing axis has been imposed basing on typical values reported in literature [28].

Finally, due to the low AoA that guarantees the achievement of the estimated cruise lift coefficient

(see 7.2.1), no incidence angle has been set for the wing. Instead, from *xflr5* simulations, the zero-lift AoA resulted to be $\alpha_0 = -4°$.

7.2.1 Lift enhancement and final results

In order to define the aerodynamic parameters in all the significant phases, it has been necessary to validate and integrate previous results with several simulations through a tool that allows to consider the DEP technology, together with the blown effect.

Therefore, the parametric aircraft geometry tool *OpenVSP*, released from NASA, has been involved. This software allows to create a 3D model of an aircraft defined by appropriate engineering parameters and, more precisely, the aerodynamic analysis have been carried out using *VSPAERO*. The latter is a vortex lattice solver which integrates actuator disks and discrete vortexes that are applied to each panel generated in the *OpenVSP*-DEGENERATE GEOMETRY FILE and then evaluated over the entire surface to obtain a pressure distribution, and so aerodynamic forces.

In particular, because of the changeable configuration of HExi aircraft, several simulations in four different conditions have been carried out. It has to be noticed that these parameters have been derived from a study of DEP propellers' design, together with the lift enhancement analysis explained in 6.5. This trade off led to the optimal propulsion characteristics reported in Table 15, used to define the final aerodynamic response and parameters of the aircraft.

Configuration	**DEP**			**Nose Propeller**		
	RPM	c_T	c_P	RPM	c_T	c_P
TO @ 5000 ft	5500	0.2073	0.1527	2700	0.1610	0.1549
Cruise @ 10,000 ft	-	-	-	2200	0.1068	0.1705
TD @ 5,000 ft	5000	0.2277	0.1591	Idle	0.1372	0.1927
Stall @ msl	5500	0.2486	0.1648	Idle	0.1679	0.2108

Table 15: Propulsion parameters used for the aerodynamics simulations.

Basing on aerodynamic results obtained during different simulations, it has been possible to define the final position of the DEP propellers with respect to the wing. More in details, in terms of x-position, they are located 0.32 m in front of the LE of the wing in order to allow the folding of the propellers during the cruise phase. In addition, they're placed 0.61 m under the LE and rotate of 15° with respect to the fuselage axis, as shown in Fig. 17.

Propellers pylons have been designed creating an almost airfoil shape in order to slightly improve lift capabilities of the aircraft from all the possible components.

In the end, all the simulations and sensitivity analysis carried out through *OpenVSP*, contributed to the determination of HExi's aerodynamics, reported in Table 16. As it is possible to note,

$C_{D_{0cr}} = 0.02$	$C_{D_{0TO}} = 0.085$	$C_{D_{0LND}} = 0.105$
K_{cr}	K_{TO}	K_{LND}
$C_{L_{max_{cr}}} = 1.9$	$C_{L_{max_{TO}}} = 4$	$C_{L_{max_{LND}}} = 6$
$C_{L_{cr}} = 0.23$	$C_{L_{TO}} = 3.3$	$C_{L_{TD}} = 4.87$
$\alpha_{max_{cr}}$ =19°	$\alpha_{max_{TO}}$ =20°	$\alpha_{max_{LND}}$ =19.5°
α_{cr} =−1°	α_{TO} =13°	$\alpha_{LND} = 14°$
$(L/D)_{max} = 27.18$	$F_{max} = 29$	$G_{max} = 61.75$

Table 16: Aerodynamics results.

the only quantity that slightly branches out the estimated value is the maximum lift coefficient that the aircraft needs to reach in the worst case (MTOW and stall velocity) that increases from 5.9 to 6.

This improvement derived from the necessity to further optimize the SMP as it will be better explained in section 8.4.1, in order to overcome the 4% increment of the aircraft total mass that comes from the post-processing design and mass break-down.

The latter variation didn't modify nor the outlines of the optimizator code neither the propellers design and the aircraft results still capable of flying the mission.

Consequently, all design hypothesis and requirements in terms of aerodynamics and mission completion have been satisfied and Fig.34 in section 8.4.1 shows the definitive design point.

In Fig. 25, the real polar of HExi is reported, together with $(L/D)_{max}$, F_{max} and G_{max}.

Finally, the stall AoA estimated for TO and LND phases results higher than the values that would be reached without the implementation of the DEP. In particular, by considering the method explained in [7], it has been possible to calculate the global velocity that flows over the wing increasing both the AoA and the aerodynamics coefficients. The latter results as a combination of airspeed and velocity induced by the propellers, turning out the blown effect and allowing the estimation of the AoA increment. This computation has been simulated with *xflr5* and verified through *OpenVSP* to determine the final values reported in Table 16.

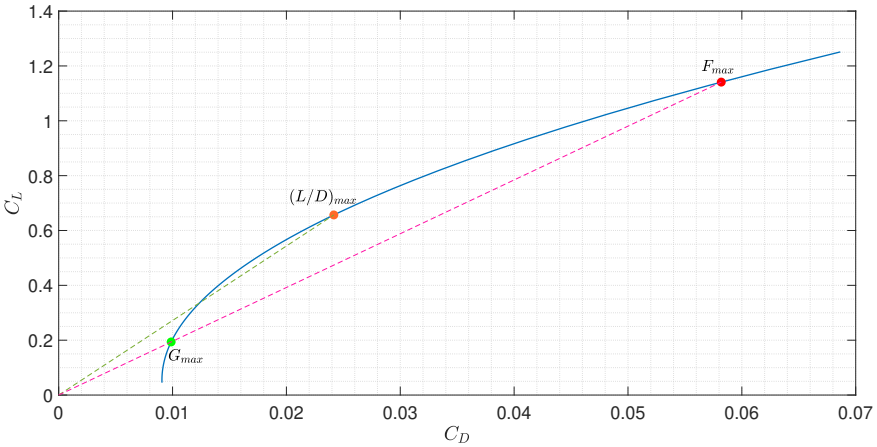

Figure 25: HExi real polar curve.

7.2.2 High lift devices

Due to the realisation of the blown effect, a complex high-lift device isn't necessary to achieve aerodynamic requirements. Therefore, a plain flap has been chosen to be installed along the trailing edge of the wing. This component cover almost the 60% of the wing:approximately from the end of the wing-fuselage intersection and the end of the rectangular portion of the wing. As reported in literature, usually the 25% of the wing mean aerodynamic chord is occupied by the flaps. Therefore, through the software *xflr5* different simulations on the increment of the lift and drag coefficient have been carried on for different flaps deflections. Results are presented in Table 17, by considering a constant flap deflection equal to δ_f =30°.

$\mathbf{c_f/MAC}$	$\mathbf{C_{lmax}}$	$\mathbf{C_d(C_{lmax})}$
0.20	2.2171	0.0950
0.25	2.2358	0.1078
0.30	2.2171	0.0950

Table 17: Aerodynamics coefficients with respect to flap chord-wise location.

From latter studies it is possible to notice that there aren't significance changes on aerodynamic coefficients. Therefore, the suggested chord-wise location for the flaps has been considered, by favoring the highest $C_{l_{max}}$. This decision followed the necessity of guaranteeing the highest possible starting value on which based the computation of the lift enhancement due to the wing-blown for designing the DEP's propellers. The latter implementation will be better explained in 6.5. Once the chord-wise location has been confirmed, the increment on lift coefficient for

different flaps deflection has been determined and it is shown in Fig.26.

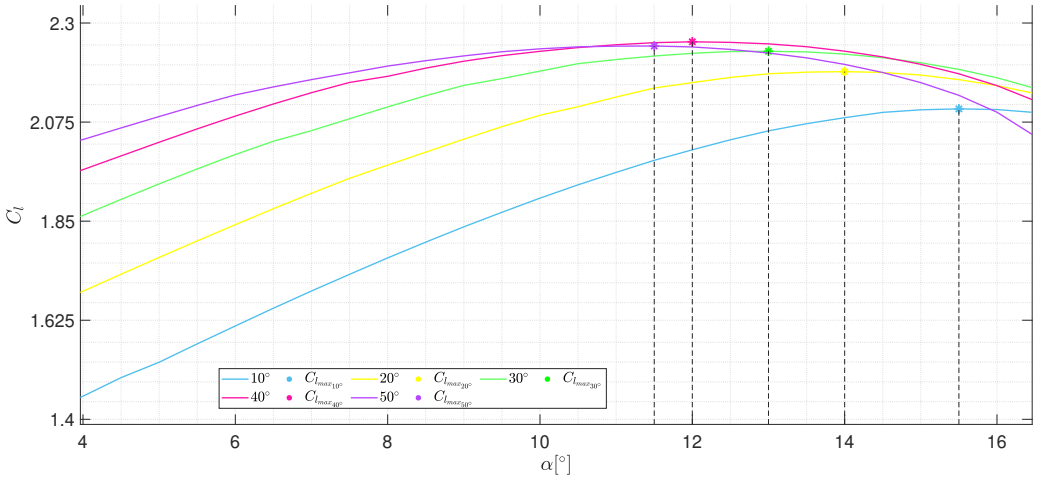

Figure 26: Lift coefficient enhancement for different δ_f.

It is noticeable that for $\delta_f \geq 40°$ the aerodynamics improvement tends to settle and then it start degrading over $\delta_f \cong 50°$. This is surely due to the fact that increasing flap deflection doesn't bring to better results every time: the wider the deflection, the lower the angle of stall, because the flow separation is earlier encountered, due to the simple architecture of the device under examination.

Therefore, through *OpenVSP* simulations it has been determined that plain flaps deflected of 20° and 30° respectively for TO and LND phases, together with the blown effect, allow to reach the high values of C_L and C_{D_0} imposed by the preliminary design studies.

7.3 Tail design

At this point, it has been possible to design a first version of the tail following the procedure suggested in [16].

7.3.1 Tail airfoil selection

First of all, it has been necessary to select the best airfoils as well for the horizontal tail as for the vertical one. Exactly as for the wing case, two lists of possible airfoils have been created and consequently evaluated with two AHP.

Only NACA profiles have been considered and, in particular, NACA profiles with 2% thickness

wrt MAC, as reported in [16] as an optimal choice. Moreover, in order to obtain good aerodynamics results, only symmetric airfoils have been taken into account for the vertical tail, as suggested in literature [16]. Finally, the following lists were obtained.

7.3.2 Horizontal tail

List of selected airfoils: NACA 0008, NACA 0009, NACA 0010, NACA 64A010. Constraints for the implementation of the AHP:

- $C_{l_{max}}$;
- minimum C_{D0};
- greater stall α;
- greater C_{L_α};
- pitching moment coefficient

7.3.3 Vertical tail

List of selected airfoils: NACA 0008, NACA 0009, NACA 0010, NACA 64A010. Constraints for the implementation of the AHP:

- $C_{l_{max}}$
- minimum C_{D0}
- grater stall α;
- greater C_{L_α}

As in the case of the wing, the analysis of the airfoils has been conducted with *xflr5*, by considering the characteristics airspeed at which the aircraft flies: Re = 6E+06 and M = 0.2. From the AHP analysis the resulting airfoils are NACA 64A010 for the horizontal tail (Fig.27) and NACA 0010 for the vertical one (Fig.28).

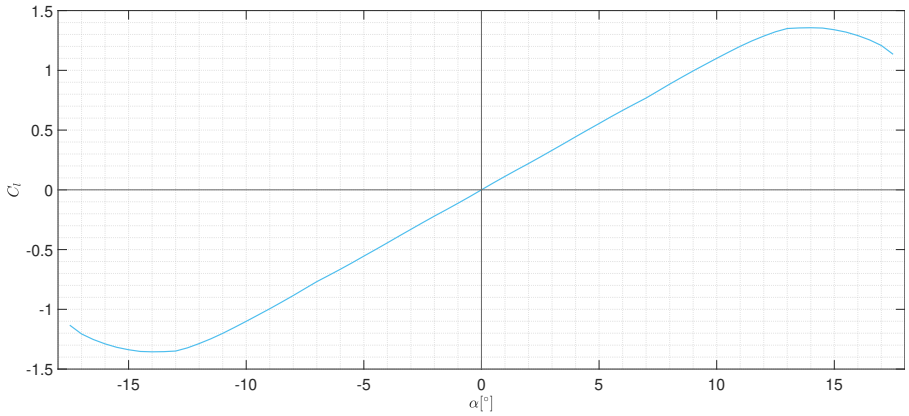

Figure 27: $C_l\alpha$ for NACA 64A010.

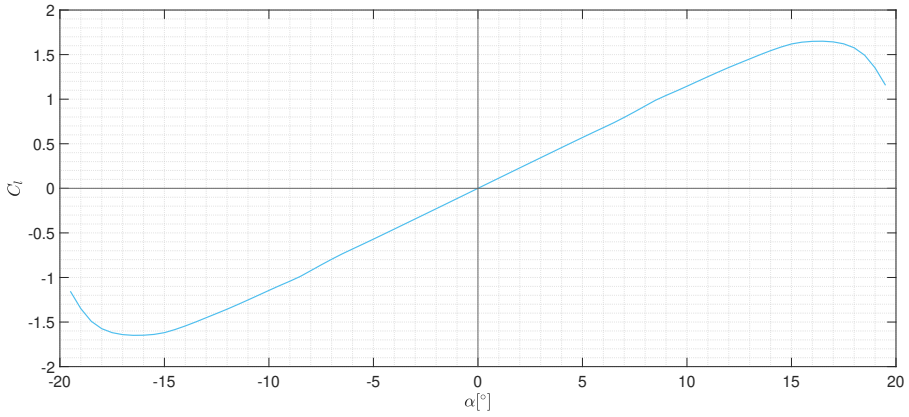

Figure 28: $C_l\alpha$ for NACA 0010.

7.3.4 Horizontal and Vertical Tail Sizing

Still basing on [16], a *MATLAB* code has been implemented in order to calculate aerodynamics and geometric parameters. Particularly, it has been necessary to set the following input parameters:

Horizontal tail:

- horizontal tail volume coefficient $V_H = 0.6$, found as typical value for horizontal tails;
- $l_h = 6.05m$, the distance between the wing LE and the horizontal tail LE and it has been found from geometric considerations through *OpenVSP*;
- $\eta_h = 0.9$, found as typical value for horizontal tails;
- $\lambda_v = 0.7$, found as optimal configuration after geometric and aerodynamics considerations with *OpenVSP*;
- $AR_h = \frac{2}{3}AR$, found as optimal AR_h

Vertical tail:

- vertical tail volume coefficient $V_V = 0.04$, as suggested typical value;
- $l_v = 5.75m$, the distance between the wing LE and the vertical tail LE. It has been derived from geometric considerations made through *OpenVSP*;
- $\lambda_v = 0.8$, found as optimal configuration after geometric and aerodynamics considerations through *OpenVSP*;
- $AR_v = 1.3$, found as optimal AR after geometric and aerodynamics considerations in *OpenVSP*;

At this point, a lifting line theory analysis has been implemented and results were validated with the help of *xflr5* and they are reported in Table 18.

	Horizontal Tail	**Vertical Tail**
Surface	2.03 m^2	1.18 m^2
Span	3.38 m^2	1.24 m^2
Mean Aerodynamic Chord	0.60 m	0.96 m

Table 18: Horizontal and Vertical Tail Data.

7.4 Primary flight Control Surfaces

Ailerons, elevator and rudder have been implemented through a *MATLAB* code following [16] and consequently results have been validated with *xflr5* and *OpenVSP* analysis.

7.4.1 Ailerons

The aileron architecture covers the tapered part of the wing (40% of the semi-span of the wing) until the wing tip, verifying the typical percentage for ailerons span. In terms of chord-wise location, the primary control surface under study covers $25\%MAC$, as the flaps system. The designed geometry (obtained values are reported in Table 19) has been confirmed from stability studies section 10, from which resulted an up and down deflection of $\delta_{A,max} = \pm 20°$, remaining below the typical maximum value of $\pm 25°$.

Together with stability, ailerons have a strong impact also on the roll controllability of the aircraft. Related to this latter aspect, an important feature on which ailerons act is the maximum force supported by the pilot. However, in HExi configuration, it is assured by the utilisation of a fly-by-wire system as explained in section 9. Indeed, it can be derived as $F_s = G_c \cdot H$, where $G_c = \frac{\delta_A}{x_s}$. In the latter formula, x_s denotes the linear mechanical movement of the stick, that in HExi design is substituted by the fly-by-wire and H identifies the Hinge moment. In particular, thanks to the latter system on-board, the actuator and redundancy of the aileron is guaranteed, allowing an higher level of safety for this primary control surface.

7.4.2 Elevator

Elevator is a primary control surface, through the deflection of which longitudinal control is applied. Assuming longitudinal control uncoupled from lateral-directional one, the design of the elevator results to be independent from the one of ailerons and rudder. A *MATLAB* code has been implemented and multiple analysis have been conducted considering the ratio b_E/b_h equal to 1, 0.8, 0.75 or 0.70 with a maximum elevator deflection $\delta_{E,max}$ =20° (conventionally the up deflection of elevator as negative, and the down deflection as positive). The analysis of these different airfoils has been carried out with *xflr5* by considering the same Re and M numbers implemented for the tail and wing analysis.

Finally, results for the optimal configuration are reported in Table 19.

7.4.3 Rudder

Rudder is a primary control surface, through the deflection of which directional control is applied. It is located on the trailing edge of the vertical tail and its parameters are determined by the directional trim and control requirements. As for the elevator case, a *MATLAB* code has been implemented in order to calculate the parameters of the rudder. Multiple analysis have been conducted considering the ratio b_R/b_h equal to 1, 0.8, 0.75 or 0.70 with a maximum rudder deflection $\delta_{R,max} = \pm 20°$. Analysing these different configurations with the help of *xflr5* (with the same settings as for the elevator case) the optimal configuration resulted to be for $b_R/b_h = 0.7$. The other data are available in Table 19.

	Ailerons	**Elevator**	**Rudder**
Surface Ratio	$S_A/S = 0.05$	$S_E/S_h = 0.2$	$S_R/S_v = 0.18$
Span Ratio	$b_A/b = 0.4$	$b_E/b_h = 0.4$	$b_R/b_v = 0.7$
Mean Aerodynamic Chord Ratio	$c_A/c = 0.25$	$c_E/c_h = 0.25$	$c_R/c_h = 0.25$

Table 19: Control Surfaces Data.

8 Structural design

8.1 Fuselage

Fuselage design has started by evaluating requirements in terms of aerodynamics and internal space.

In order to comply with aerodynamic requirements on C_{D_0} in cruise condition (4.1), the fuselage has been modeled with a tadpole shape.

With this particular kind of shape it is possible to reduce drag because the airflow can be maintained as laminar for a big portion of its length. After the transition to a turbulent flow, the empennage section is drastically reduced limiting negative effects due to turbulent flow's pressure raise.

For security reasons the cockpit's area has been separated from passengers' area and the pilot sits alone at the front of the cabin.

In order to accommodate the passengers, a 1 - 2 layout has been selected so that there is space for a cockpit door next to the single seat.

Passengers' luggage are stored in a designated storing space at the end of the cabin. This choice was necessary since the internal space in the cabin wasn't sufficient to respect volume requirements imposed for luggage. A graphical representation of the fuselage shape is shown in Fig. 29.

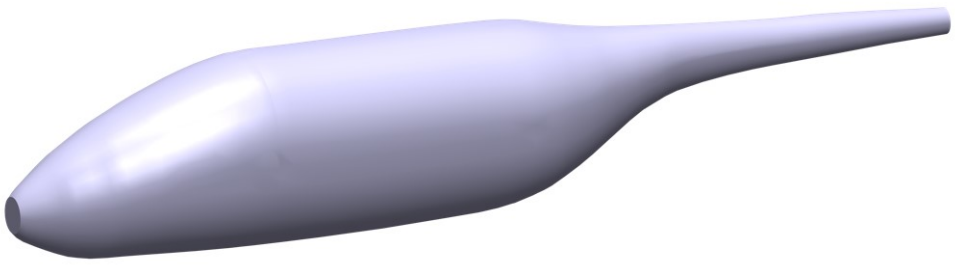

Figure 29: Shape of the fuselage.

8.2 Landing gear

Given the overall shape of the aircraft, the position and excursion of the aircraft center of gravity, the design of the nose and main landing gears has been carried out, by following the methodology described in [28].

One of the most stringent requirements in the design of the landing gear, is the aircraft capability to take off and land on dirt, grass, metal mat, gravel, asphalt and concrete runways. Different landing gear configurations have been analyzed but, among all, the two most promising ones have been turned out to be the taildragger and tricycle configurations.

The latter one has been finally selected mainly to guarantee the best comfort to passengers, since the floor deck angle is closer to being horizontal and the touchdown results to be less bouncy with respect to taildraggers. Even if this choice is more expensive, it guarantees also a greater visibility to the pilot and a better ground controllability.

Another fundamental aspect to consider in the early stages of the landing gear design, is the choice of a fixed, retractable, or partially retractable configuration. After a series of aerodynamic simulations, a fully retractable gear configuration has been chosen, due to the induced drag coefficient reduction, enabling a high performance aerodynamic behaviour in cruise.

The resulting landing gear is a retractable, tricycle type with a steerable nose wheel and two main wheels. Given the initial configuration choice, an iterative geometric design procedure has been performed through the use of *SolidWorks* and *MATLAB*. An example of such process is shown in in Fig. 30.

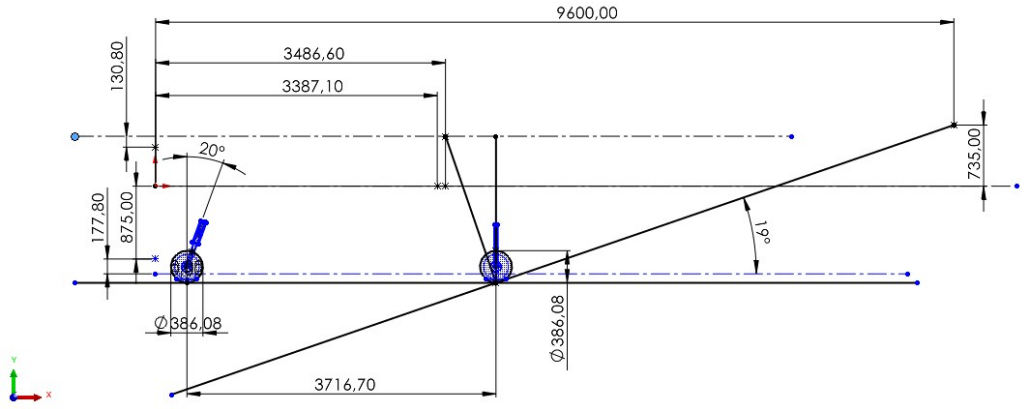

Figure 30: Landing Gear design step.

The inputs of the design procedure are the longitudinal forward and aft position of the center of

gravity and its vertical location, as well as the position of the horizontal tail and of the nose propeller. These data have been used to prevent the aircraft tipback and prop-strike. Once the position of the main gear has been chosen, the nose gear has been positioned in order to properly carry the amount of load and maintain the aircraft static stability.

Throughout the entire design process, a MTOW increased of the 25% with respect to the estimated value has been considered. This choice is based on the hypothesis of a successful production and a consequent request for added capabilities on new models that would lead to costly re-engineering.

Once the aircraft wheel track and wheel base have been determined, the requirement on the overturn angle has been checked.

Finally, the last step of the design process involved the determination of the loads and tires on each gear strut as well as the position of the gears when retracted.

After computing the main gear static and nose gear maximum dynamic loads, the final tyre chosen for HExi turned out to be the Goodyear Rib Tube Type 385M61-1.

This tyres allow the aircraft to land on unprepared runways due to its low inflation pressure. Each main wheel is equipped with a hydraulically actuated disc-type brake on the inboard side of the wheel. Shock absorption is provided by the leaf type spring-steel main landing gear struts and the air/oil nose gear shock strut. This architecture has been selected due to its lightweight and easy to store properties. In particular, the entire main gear and nose gear can be retracted rearward and upward into the belly of the aircraft, covered by the wheel well doors. An example of a similar retraction mechanism may be found in the Cessna 337 Skymaster although the nose gear is retracted forward.

Though this class of aircraft couples electric and hydraulic systems in the retraction dynamics, for HExi a full electric motion has been hypothesized, after a careful analysis of the forces involved and the power required.

The main characteristics of the landing gear structure, tires and brakes are collected in Table. 20.

Main landing gear position wrt to main propeller	4.09 m
Nose landing gear position wrt to main propeller	0.57 m
Minimum ground-fuselage distance	0.66 m
Wheel track	2.67 m
Wheel base	3.72 m
Tires part number	385M61-1
Rated inflation	45 PSI
Maximum braking load	10320 N

Table 20: Landing gear data.

8.3 Materials

Due to the light weight estimated from preliminary studies, it has been decided to take advantage of composite materials. This decision has also been based on the particular shape of the fuselage, that has been thought to guarantee an easier and efficient pressurization process. In particular, for the main part of the aircraft, the HexPly 8552 UD Carbon Prepregs, with carbon fiber (PAN) IM7-G,12k has been selected. This choice derived from several trade studies among the different existing composite materials for aerospace applications.

First of all, the fatigue response of the structure has been considered as one of the most significant constraints on material selection. Therefore, the decision has been limited to HS carbon fiber of type PAN.

Moreover, the light weight has imposed the selection of a material with the lowest possible density value. Consequently, by matching the preceding main constraints, the composite material previously mentioned won the selection.

More in details, HexTow IM7 carbon fiber is a continuous, high performance, intermediate modulus, PAN based fiber. In addition, its unique properties, such as higher strength and modulus, as well as good shear strength, allow the achievement of higher safety margins for both stiffness and strength critical applications.

Surely, due to the sensitivity of the materials under examination, special treatments of those regions where holes or discontinuities are presented have been taken into account. Close to this lightness characteristic, a reinforcement on the bottom region of the fuselage has been considered. In particular, HS aramid fiber reinforced plastic have been selected.

The properties of the materials under examination are listed in Table 21.

Material	ρ[kg/m^3] fiber	ρ[kg/m^3] resin	E [GPa]	σ_b [GPa]	ϵ_u at Failure%
HexPly 8552 UD	1770	1300	228	5.655	1.9
HS aramid fiber	1500	-	280	5.7	2

Table 21: Materials properties.

8.4 Structural Sizing

Given the overall aircraft geometry, the preliminary guess of weight components and configuration, as well as the complete aerodynamic configuration,it is possible to carry out the structural analysis. Many of the load factors and speed limits are defined from regulations, where prescribed test cases are used to assess the compliance of the aircraft under all possible operative loading conditions.

The suite used to perform such calculations is *NeoCASS*, a freely distributed package for preliminary structural design and analysis developed at Politecnico di Milano. This tool gives as outputs a complete structural sizing compliant with regulation requirements and a stick model suitable for aero-elastic analysis.

As a first step, the geometric layout has been developed through the module ACBUILDER, by taking into consideration both distributed and concentrated masses.

Consequently, the structural shape of the aircraft and the material have been defined, so the centers of gravity and the components' mass.

More precisely, the parameters reported in Table 22 have been imposed, by selecting typical values suggested in [5].

Spar location (tip − root)	Rib location
(0.15 − 0.55)c	36 inches

Table 22: Wing cross-section geometry.

Once the model has been defined, through the module called GUESS, different maneuvers have been selected in order to study the structural response of the airplane. The examined conditions are reported in Table 23. Note that *NeoCASS* allows to select automatically the certification that the design has to follow. However, only EASA regulations are available, therefore, the equivalent to the FAR-23, CS-23, has been selected in order to proceed with the analysis.

ID	**Maneuver**
$1-4$	Maximum load factor @ V_D and V_C
$5-6$	Cruise and gust for LND @ V_F
$7-12$	Sudden aft movement of the pitch control @ V_A, V_C and V_D
$13-24$	Sideslip
$25-28$	Aileron adrupt
$29-31$	Gust
32	Tail down landing

Table 23: Analysed Maneuvers.

As a first trim analysis, in Fig.31 the Placard diagram is reported. It allows to have a global idea of the evolution of the airspeed with the increment of the altitude, until the maximum operating one, set to 15,000 ft [3] in order to satisfy the requirement from RFP.

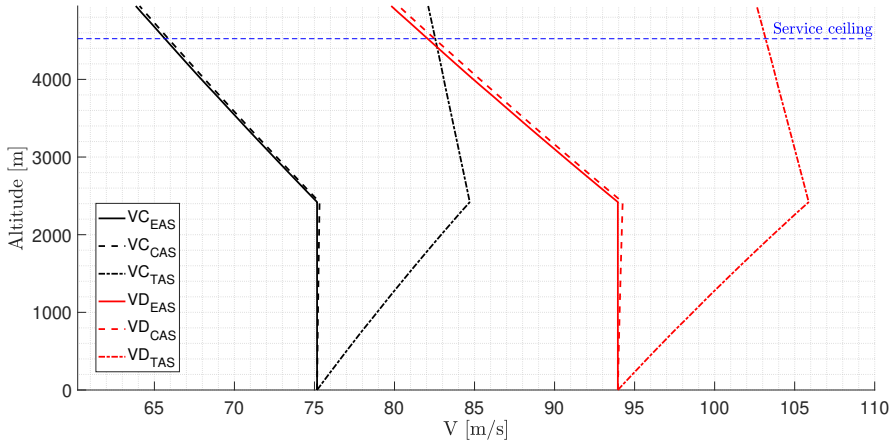

Figure 31: Placard diagram.

In particular, both the cruise and the dive speed can be visualized, in terms of EAS, CAS and TAS. As expected, the latter is the higher one and up to the cruise altitude the airspeed increases until the target one is reached. On the other hand, by definition, EAS and CAS

[3]Note that *NeoCASS* has been implemented based on the measurements SI, therefore on the graphs all the quantities are reported in SI.

airspeed remain constant with respect to the altitude growth.

An other important diagram that can be visualized from the GUESS module is the V-n diagram, shown in Fig. 32. Nevertheless, only the positive portion can be obtained, therefore, the reported diagram in Fig.32 has been obtained following the procedure explained in [5]. This diagram shows the safe flight envelope in terms of load factor with respect to airspeed. It is limited on the y-axis by the maximum value of the load factor given by structural limitations. For low speeds, instead, it is limited by stalling condition considering the maximum load factor defined. At high speeds, finally, the limitation is given by the dive speed, V_D, defined as $V_D = 1.25 \cdot V_c$ where V_c is the design cruise speed. The resulting V_D is equal to $V_D = 182$ KEAS.

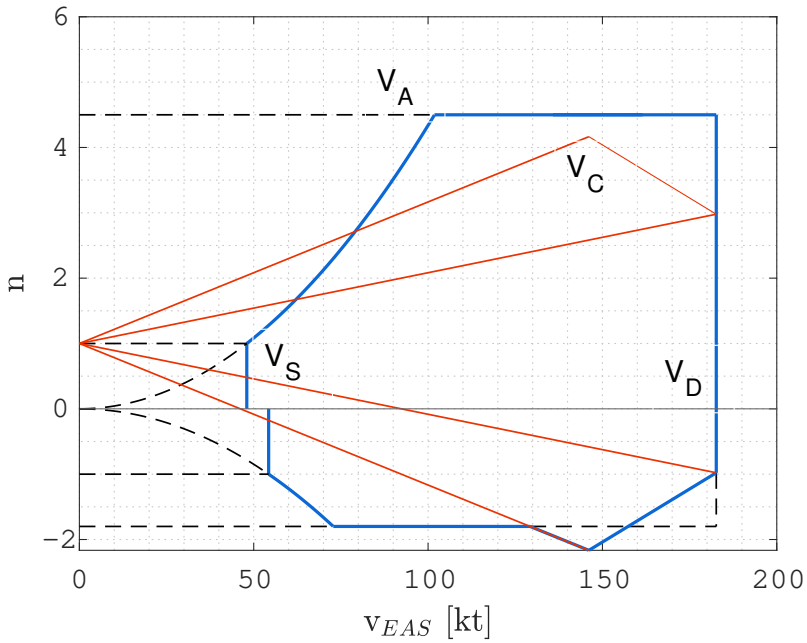

Figure 32: $V - n$ diagram.

Finally, in Fig.33[4], the stick model of the aircraft is presented.

[4]Note that some of the DEP propellers can't be visualized in the figure. This is due to the fact that they are defined as "added masses", that are not graphically shown by the tool.

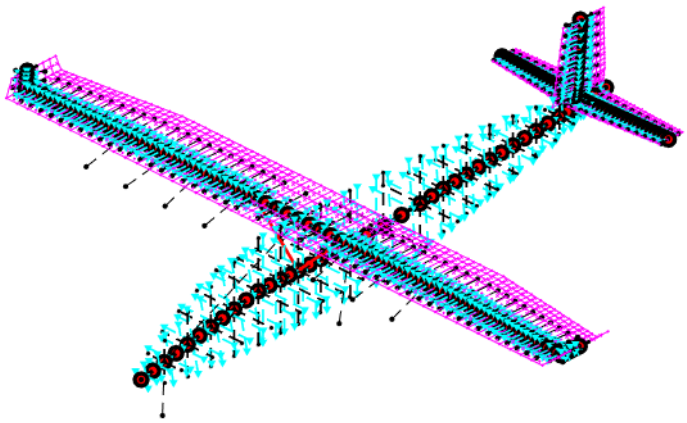

Figure 33: Aircraft Stick Model.

8.4.1 Mass brake-down and loads

Masses of the main structural components and systems have been estimated using the method presented in [16].

A detailed table (24) containing the resulting masses obtained will be presented later in section 10. From the latter values it is clear that the MTOW is slightly grater than the mass estimated in the preliminary design. Therefore, the final design point is reported in Fig.34 (that represents a short-cut of Fig.6).

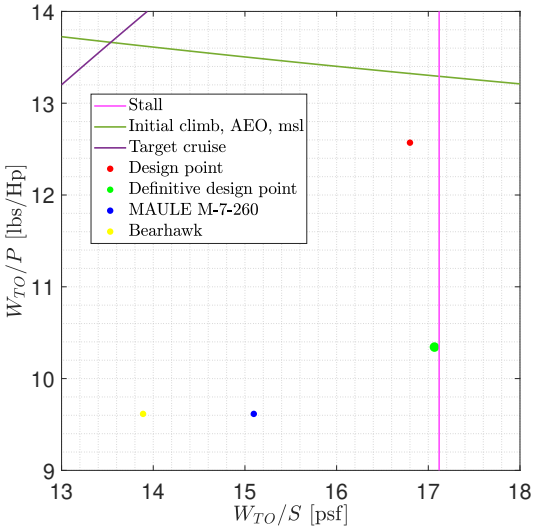

Figure 34: Final SMP.

In terms of mass distribution, the static analysis developed in the SMARTCAD module allowed to obtain the trend of the mass-ratio with respect to MTOW along fuselage and wing axis, as reported in Fig. 35.

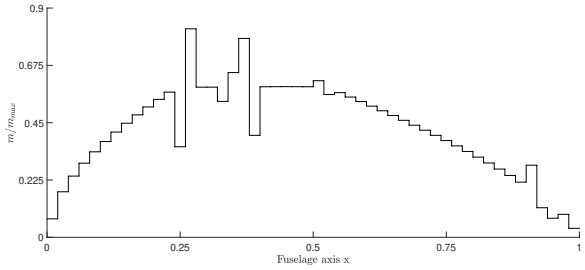

(a) Fuselage mass distribution.

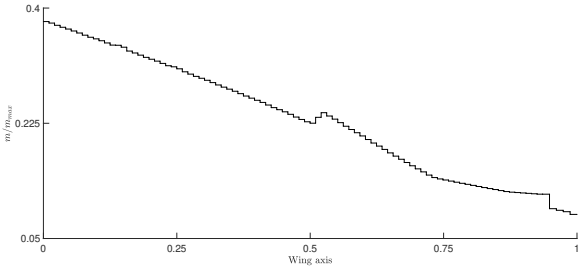

(b) Wing mass distribution.

Figure 35: Fuselage and wing mass distribution.

Basing on previous graphs, in Fig.36 are shown different loads for each maneuver established at the beginning of the analysis.

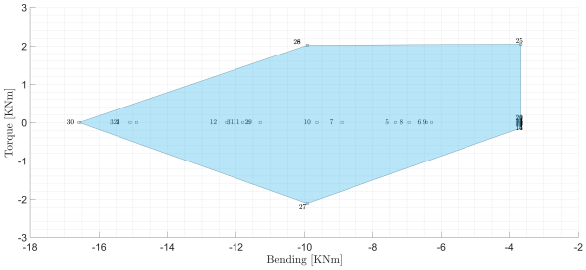

(a) Fuselage banding VS torque.

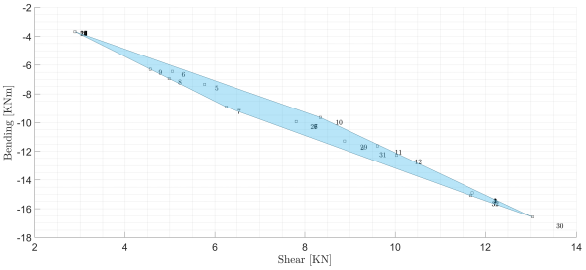

(b) Fuselage shear VS bending.

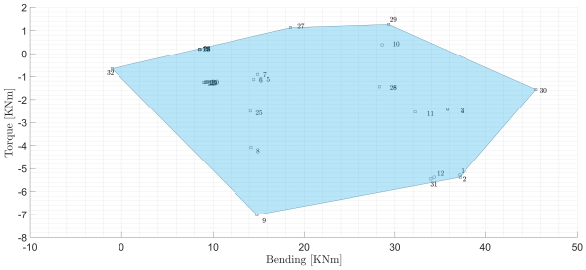

(c) Wing bending VS torque.

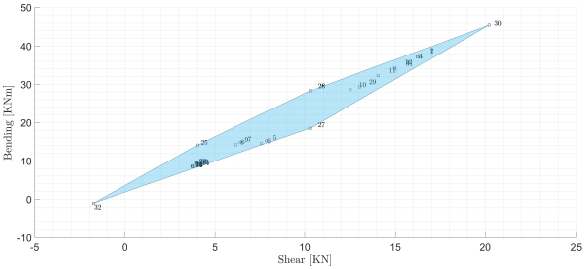

(d) Wing shear VS torque.

Figure 36: Fuselage and wing loads.

More precisely, for the wing, the considered node is at the 5% of the span and so in the region close to the intersection with the fuselage, where loads are expected to be higher.
Instead, in the case of the fuselage, the 30% of its axis has been considered for the analysis, because its neighbourhood determines the most loaded part of the component under examination.

8.4.2 Flutter analysis

Finally, in terms of modal response, flutter analysis surely requires attention, being an important study on the aircraft design process.
Through the SMARTCAD module, after having analysed the static response, the modal one has been carried out. In particular, 20 modes have been studied: 6 of them resulted as rigid modes and the remaining 14 as deformative. As it can be visualized in Fig.37, both the frequency and damping behaviours with respect to velocity are reported, for each deformation mode.

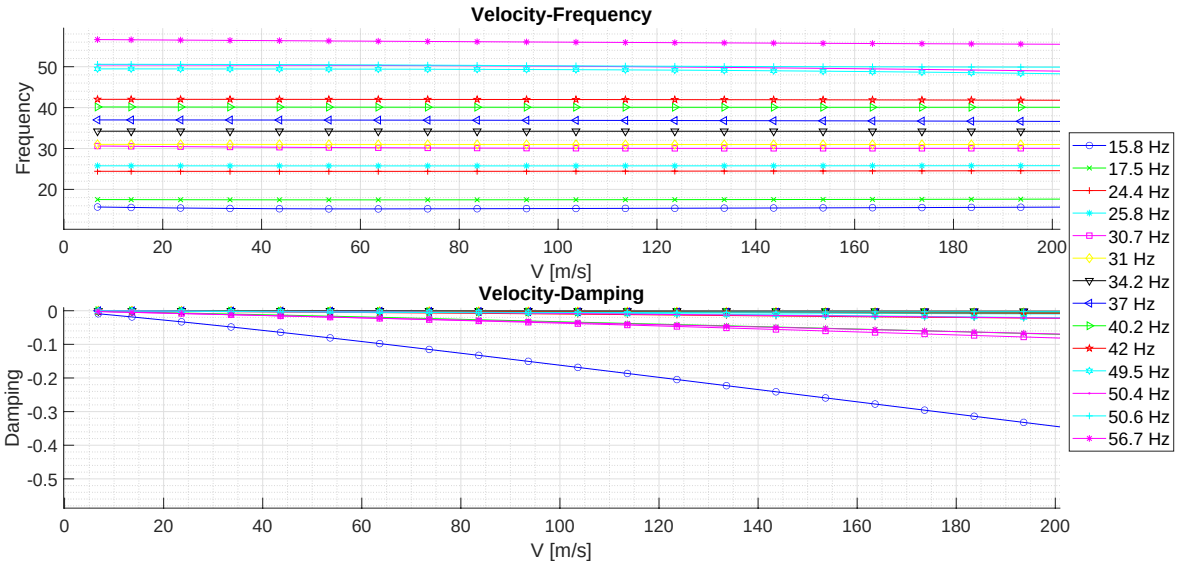

Figure 37: Frequency and dumping ratio.

As also resulted at the end of the analysis carried out in *MATLAB*, no flutter is detected. This is confirmed from the negative damping ratio obtained by the analysis. On the other hand, frequency behavior needs a slightly deeper attention. Looking at Fig.37, by starting from the top of the graph, the second two frequencies at the lowest velocities are almost overlapped. Therefore, in a more advanced phase of the aircraft design process, it will surely be necessary to pay particular attention to these two modes.

8.5 HExi geometry

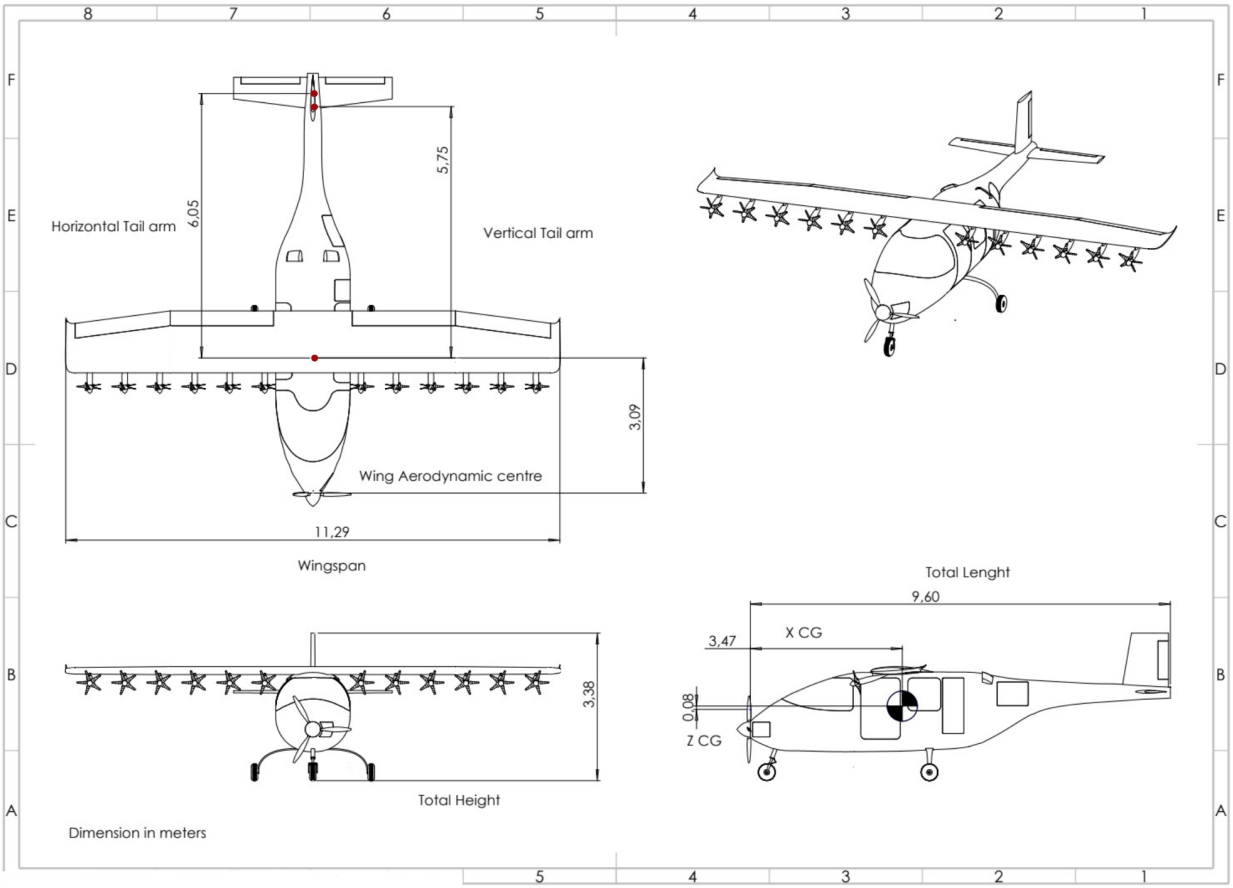

Figure 38: View from three sides of HExi.

9 Systems

9.1 Power Management And Distribution

The PMAD system has the function to transfer the generated power in a safe and redundant way. The electric generator is coupled with a rectifier that convert AC in DC. Circuit brakers and fault-current limiters, placed upstream of any electric component, are used as main protection devices. DC electric motors used for DEP are piloted through electronic speed controllers.

9.2 Avionics

HExi is equipped with new-generation avionics that improve pilot situational awareness and provide in-cockpit information about traffic, weather, airspace and terrain. The main systems installed in the cabin are:

- touchscreen flight display (G500 TXi 7" Landscape display);

- touchscreen flight navigator (GTN 750Xi);

- digital autopilot (GFC 500).

Together with the fly-by-wire system, they guarantee to perform both visual and instrument flight. The avionic systems chosen are integrated in order to offer a high level autopilot capable of flying in IFR condition in all airspace classes. Redundancy is obtained by the installation of two flight control computers.
The flight management system is responsible to switch from pure electric to hybrid electric propulsion and vice versa on the basis of the level of charge of the batteries and the phase of the mission. However a physical switch is present in the cockpit as a backup.

9.3 Fuel system

The fuel is stocked in two integral rectangular tanks, one per wing, positioned as close as possible to the longitudinal axis of the aircraft: in particular, the closest side is far 1 m to the axis.

Integral tanks have been selected because they provide the highest volume of space available with the lowest weight. They measure 1.50 m long, 0.40 m wide and 0.10 m high and their x-center of gravity correspond to the wing's one.
Finally, three pumps are installed on the fuel system lines:

- center line pump: it allows the connection between the two tanks in order to guarantee a constantly fuel balance;
- one for the right tank line and one for the left one: these pumps permit the connection between each tank and the ICE.

The scheme of the fuel lines can be visualized in Fig. 39.

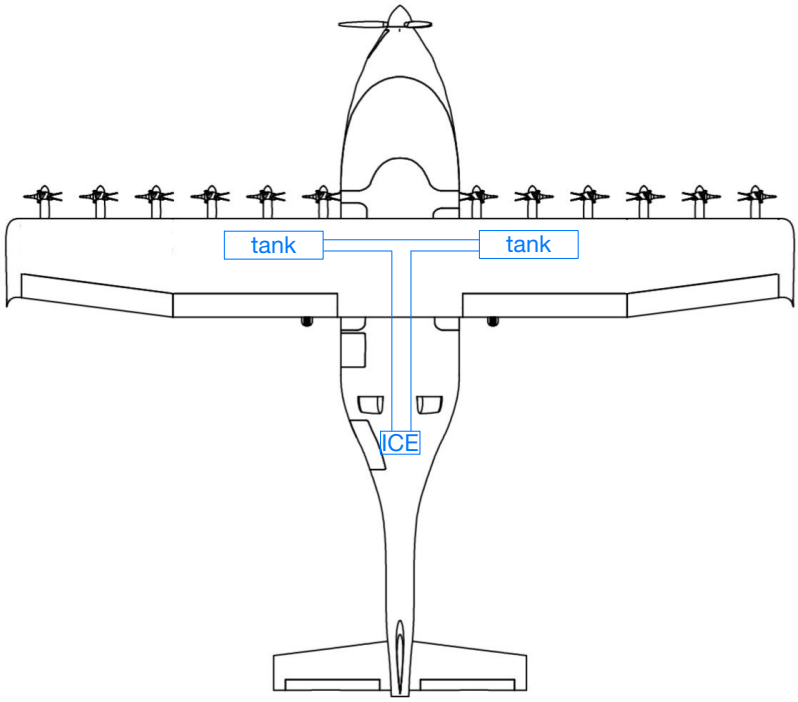

Figure 39: Fuel system lines.

9.4 De-icing system

An analysis has been conducted on aircraft similar to HExi in terms of size, weight and range, and equipped to fly in icing conditions. The most common ice protection system between the aircraft considered turns out to be the pneumatic boot system, which consists in a de-icing system whereas anti-icing systems are rare for these aircraft. For these reasons HExi is equipped with just the boot system, that warranties for safe operations. Boots are installed on the leading

edge of wing and tails, since these areas are most likely to accumulate ice that could severely affect the aircraft's performance.

Finally, the air-born system is matched with both aircraft ground de-icing and anti-icing procedures that are conducted suddenly before take-off in order to remove any form of ice from critical external surfaces and fan blades, whenever there are extreme low temperature conditions.

9.5 Environmental control system

A pressurization system is installed since HExi will fly at altitudes above 10,000 ft. In particular the maximum operating altitude is set to 15,000 ft in order to guarantee a 14,000 ft service ceiling as requested from the RFP.

The system under examination is necessary to protect the pilot and passengers against excessive pressure gap that would lead to serious health issues.

More precisely, the turbocharger of the main propeller is used as source of pressurization.

Moreover, cabin pressurisation is achieved by a cabin pressure control valve installed in the cabin wall and controlled by the Environmental Control System (ECS). It sets the cabin pressure to the required value, depending on the altitude, by regulating the flow of air from the cabin. In the case of a pressurization loss, the cabin pressure control valve will be closed.

Non-return valves are installed in the air distribution pipes so that when the air supply fails, the air already in the cabin can't leak back out through the pipes.

In addition, a safety valve is installed in the cabin wall to relieve internal pressure if it increases above a certain value in the event of a pressure control valve failure.

Finally, an emergency oxygen system is installed to guarantee a safe flight in case of contamination of the cabin air by smoke and fumes or by a pressurization system failure.

9.6 Anti-collision and anti-bird-strike system

Urban air mobility is expected to grow fast in the next years so the air traffic. To guarantee safety on flight, a Traffic Collision Avoidance System (TCAS) is installed. TCAS is also employed as bird-strike avoidance system since HExi has to be able to operate in very different environmental scenario, both in terms of runways and geographical areas. These environments are potentially hazardous for the great presence of birds, more than typical airports where

ground infrastructures are installed to drive-away birds.

9.7 Future developments: Unmanned operations

The previsions made in section 3.7 could lead to a possible overcrowding of the airspace in cities. A possible solution of this problem could be the introduction of unmanned vehicles, once adequate margins on their robustness and safety are reached. At this stage, unmanned aircraft cannot be certified under civil regulations. Nonetheless, with the rapid development of autonomous systems seen in the mobility business, it is very likely that in a near future this technologies could be applied to aircraft as well.

For these reasons, a future updated version of HExi that includes the ability to execute autonomous flight is very likely. Thanks to the implementation of a fly-by-wire architecture and already advanced flight computers, the changes required to the aircraft would be confined to an upgrade of flight computers software. In this scenario, the role of the pilot would be limited and a cockpit area would not be required. This would allow to increase the cabin volume with the possibility of transporting more passengers each flight, compromising on range, with a revised internal layout that grants stability.

10 Stability analysis

10.1 Longitudinal static stability

In order to study the longitudinal static stability of the aircraft, first of all, it has been necessary to estimate weights and dimensions of the most important systems (Table 24).

Component	Weight [kg]	X Location [m]	Z Location [m]
Wing	109.22	3.33	0.89
Horizontal Tail	6.23	9.14	0.40
Vertical Tail	3.11	9.00	1.08
Fuselage	163.15	3.53	-0.04
ICE	134.00	6.00	0.30
Batteries	85.00	2.98	-0.83
Electric Motor	21.92	0.26	-0.47
Furnishings	38.95	3.00	-0.04
Avionics	11.71	1.30	-0.42
Control System	20.15	3.33	0.89
Electric System	38.93	3.00	0.00
Air-Conditioning System	27.33	0.65	-0.60
Fuel	88.00	3.33	0.89
Fuel System	8.88	3.33	0.89
DEP	5.5·12	2.40	0.81
Baggage	3·13.61	4.58	-0.30 / 0.35
Main Landing Gear	40.59	4.09	-1.25
Nose Landing Gear	9.52	0.44	-1.26
Pilot	86.18	2.02	-0.06
Passenger 1	86.18	2.66	-0.09
Passenger 2	86.18	4.09	-0.09
Passenger 3	86.18	4.09	-0.09

Table 24: Weights and Locations.

The considered reference system (Fig.40b) has been set as follows:

- Origin in correspondence of the nose of the aircraft;
- X-axis along the roll axis of the aircraft;
- Y-axis along the pitch axis of the aircraft;
- Z-axis along the yaw axis of the aircraft

An initial layout has been proposed taking into account volume constraints inside the fuselage. Successively, the initial configuration has been iterated until obtaining the stable configuration represented in Fig.40b.

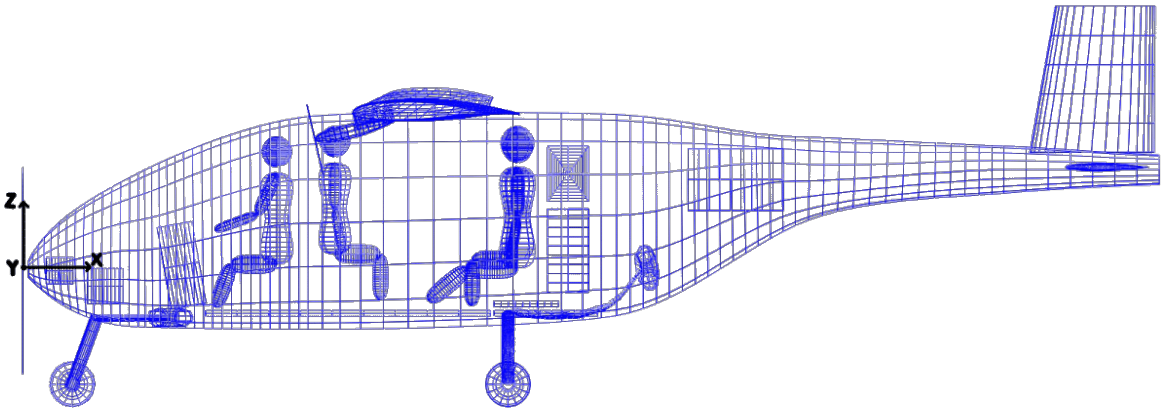

(a) Internal layout.

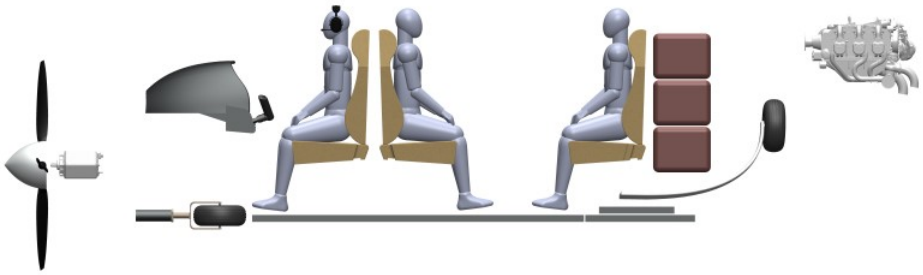

(b) Internal layout from 3D model.

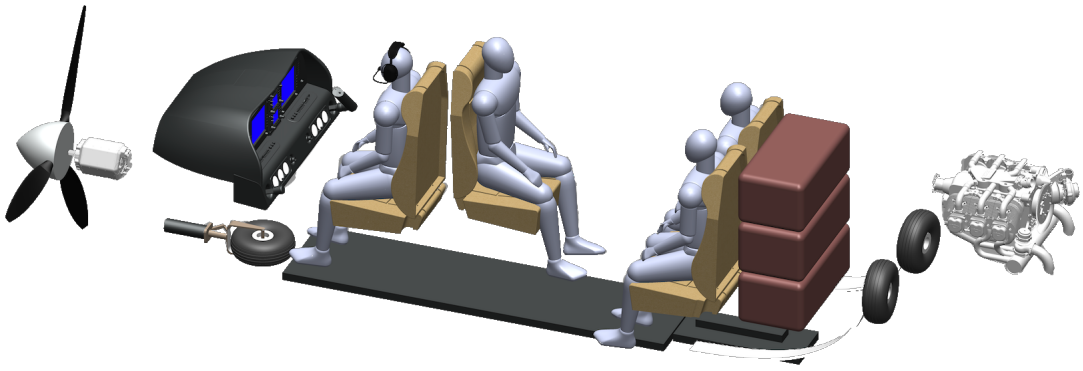

Figure 41: Internal layout.

In particular, the stability of the aircraft has been studied using both the stability margin (Eq.8) and the Borri parameter (Eq.12) considering both full fuel tank and no fuel (2% of full fuel) conditions with the following loading conditions:

- 3 passengers and pilot;
- 2 passengers and pilot;
- 1 passengers and pilot;
- Just pilot

More precisely, the stability margin is computed as follows:

$$e = \frac{X_G - X_N}{MAC} \tag{8}$$

where X_G is the barycenter of the aircraft.
X_N (Eq.9), the neutral point, is the position of the aerodynamic center for the entire aircraft:

$$X_N = \frac{X_{AC_w} \cdot C_{L_w} + \eta_h \cdot \sigma_h \cdot X_{AC_h} \cdot C_{L_h} \cdot (1 - \varepsilon_\alpha)}{C_{L_w} + \eta_h \cdot \sigma_h \cdot C_{L_h} \cdot (1 - \varepsilon_\alpha)} \tag{9}$$

On the other hand, Borri formulation defines the Control point (X_C, Eq.10) as the counterpart of the aerodynamic center but referred to the elevator deflection. It is reasonable to assume that the control point is in the close vicinity of the tail aerodynamic thus:

$$X_C = X_{AC_h} \tag{10}$$

By the definitions given of X_N and X_C, it's possible to decompose the total lift in 2 components:

- Attitude lift L_a, only function of α;
- Control lift L_{δ_e}, only function of the elevator deflection δ_e

and, by imposing the equilibrium of moments around the barycenter, to obtain the following

expressions:

$$\begin{cases} L_a = (1+\varepsilon) \cdot W \\ L_{\delta_e} = -\varepsilon \cdot W \end{cases} \tag{11}$$

where:

$$\varepsilon = \frac{X_G - X_N}{X_N - X_C} \tag{12}$$

is the Borri stability parameter.

Given that a standard configuration with rear tail has been chosen, the stability criteria for both the stability margin (Eq.8) and the Borri stability parameter (Eq.12) requires them to be positive.

Results are shown in Table 25 and, as it is possible to note, both parameters fall within the recommended ranges that are $[5\% \div 15\%]$ and $[2\% \div 3\%]$ respectively for the stability margin and Borri parameter.

Loading condition	$\mathbf{X_{CG}}$	**Stability Margin**	**Borri stability parameter**
3 passengers	3.47	10.48%	2.52%
2 passengers	3.41	14.80%	3.56%
1 passengers	3.46	11.40%	2.74%
Just pilot	3.39	16.73%	4.02%

Table 25: Stability Margin and Borri Parameter for different loading conditions.

Moreover, the longitudinal stability can be verified by computing longitudinal stability derivatives [5]. In particular, it is necessary to have $C_{\mathcal{M}_\alpha} < 0$, that is verified since the obtained value is $C_{\mathcal{M}_\alpha} = -3.41$.

10.2 Lateral directional static stability

For the lateral directional stability, it is required that:

$$\begin{cases} C_{\mathcal{L}_\beta} < 0 \\ C_{\mathcal{N}_\beta} > 0 \end{cases} \tag{13}$$

By computing these lateral-directional derivatives, the resulting values are $C_{\mathcal{L}_\beta} = -0.092$ and $C_{\mathcal{N}_\beta} = 0.03$, both satisfying stability conditions.

10.3 Crocco's diagram

As a final tool to verify stability and trim conditions, Crocco's diagram has been developed. This diagram is built considering the relation between $C_{\mathcal{M}}$, taking as a reference point the leading edge of the wing, and C_L as a function of α and δ_e.

Considering the variation of C_L obtained only by changing α, it is possible to obtain isoclinic lines.

When considering only the effect on C_L given by δ_e, instead, stick lines are obtained.

The condition of $C_L = 1$ corresponds to $C_{\mathcal{M}}$ representative of the non-dimensional position of X_{CG} with respect to MAC on the aircraft roll axis.

The line intersecting the origin of the axis and the position of the CG when $C_L = 1$ is called barycentric line. It represents the $C_{\mathcal{M}}$ required at trim condition as a function of C_L. Once the CG is known it is possible to follow the corresponding barycentric line in order to find the combination of α and δ_e that grants trim condition at the C_L required.

The considered range for α is $[-10° \div 19°]$ while the one for the equilibrator deflection is $[-25° \div 25°]$.

The CG excursion is limited in backward direction by the longitudinal stability requirement previously presented, namely the position of the neutral point. In the forward direction, instead, it is constrained by the limitation on the trim condition at the maximum α and the available maximum δ_e. This latter condition can be obtained by computing the line passing through the origin and the intersection between the isoclinic line at the maximum α and the stick line at

the maximum δ_e.

The range of CG positions obtained in section 10.1 lays inside the delimited region, verifying the requirements.

The resulting Crocco's diagram shown in Fig.42, proves that the aircraft is stable and controllable in all the loading conditions considered at cruise phase.

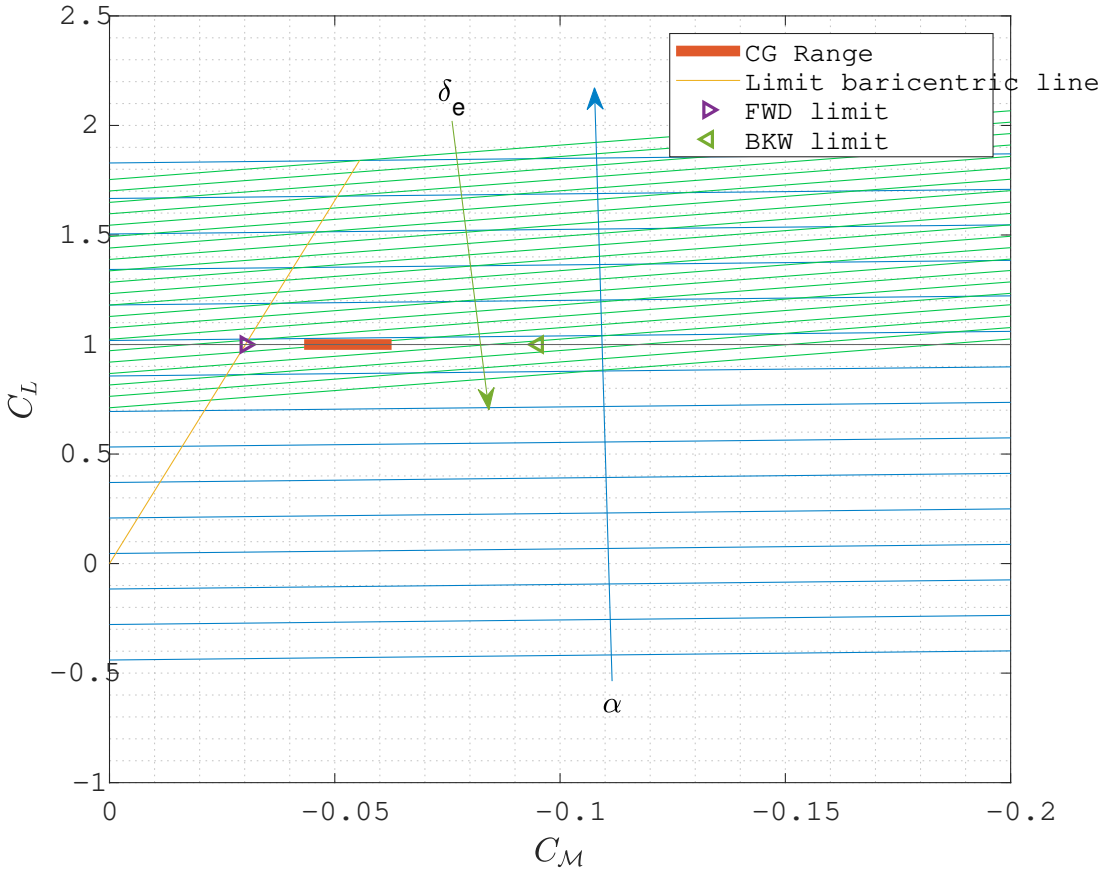

Figure 42: Crocco's diagram

10.4 Dynamic Stability

The study of dynamic stability has been done by computing the dynamic system decoupled in the longitudinal plane and in the lateral-directional plane. Stability and control derivatives have been estimated with the approach explained in [5] while an estimate of the inertial terms has been obtained with *xflr5*.

10.4.1 Longitudinal Response

The obtained longitudinal response (reported in Table 26 and shown in Fig.43) is characterized by two sets of complex conjugate eigenvalues representing the short period and the phugoid modes.

Eigenvalue	**Value**	**Damping**	**Frequency [rad/s]**
Short Period	-3.6300 + 7.84i	0.4200	8.64
	-3.6300 - 7.84i	0.420	8.64
Phugoid	-0.0082 + 0.22i	0.037	0.22
	-0.0082 + 0.22i	0.037	0.22

Table 26: Longitudinal Response.

10.4.2 Lateral Response

The lateral response (reported in Table 27 and shown in Fig.44) is composed by a set of 5 eigenvalues. Out of this 5, only 4 are relevant since the response on the yaw axis can be neglected. In particular, these 4 eigenvalues are:

- a set of 2 complex conjugate terms representing the dutch roll mode;
- a real term for the roll damping mode;
- a real term for the spiral mode.

The computed relevant modes results to be stable and positively damped as required in CFR 23 [29].

Eigenvalue	Value	Damping	Frequency [rad/s]
Dutch Roll	-0.770 + 4.57i	0.17	4.630
	-0.770 - 4.57i	0.17	4.630
Roll Damping	-10.90	1.00	10.9 0
Spiral	-0.022	1.00	0.022

Table 27: Lateral Response.

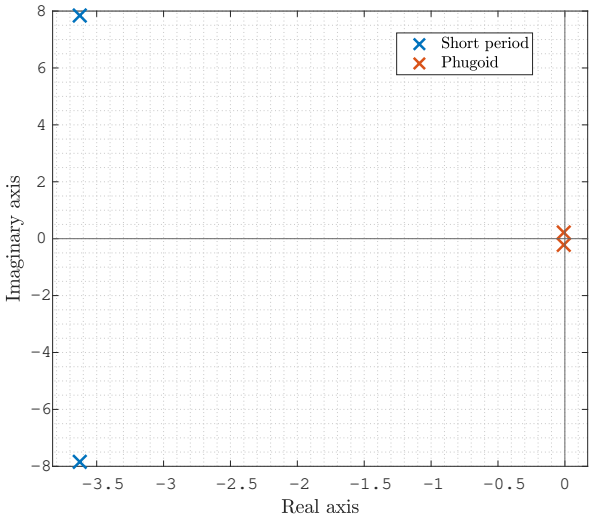

Figure 43: Longitudinal Response.

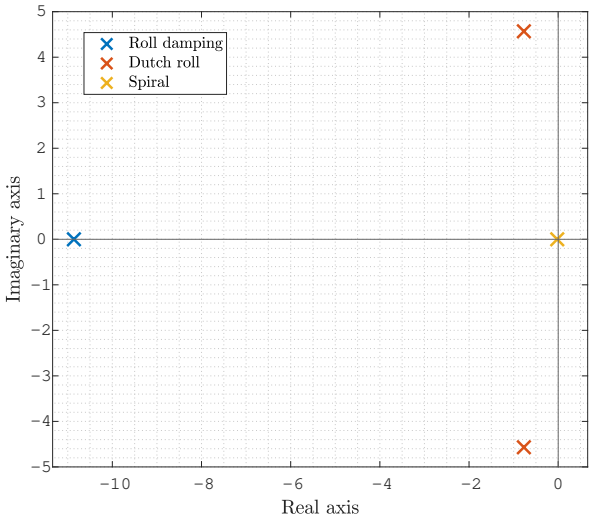

Figure 44: Lateral Response.

11 Performance analysis

In this section a description of the main performance parameters is presented.

11.1 Take Off and Landing performance

Take off distance is a strict requirement imposed by the RFP, thus it has been considered as one of the requirements imposed to the optimization code (section 4.7). Fig.45 shows the take off run (91 m) computed at 5000 ft since it is the most demanding condition in terms of required power.

However, at sea level, performances improve significantly with a take off distance of 80 m.

On one hand, from Fig.45 it's possible to see that the ground run is quite limited thanks to the increase in lift provided by the DEP. On the other hand, the airborne section required to reach the clearance of 50 ft covers the majority of the take off run despite the high initial climb angle imposed.

The same distance requirement applied to take off is also valid for landing and, similarly, the simulated landing run obtained is 90 m as shown in Fig.46. In this case, a steep angle of approach of 14° is required since, for geometric reasons, a lower angle wouldn't allow enough space for the ground run. At sea level, the landing run is equal to 87 m.

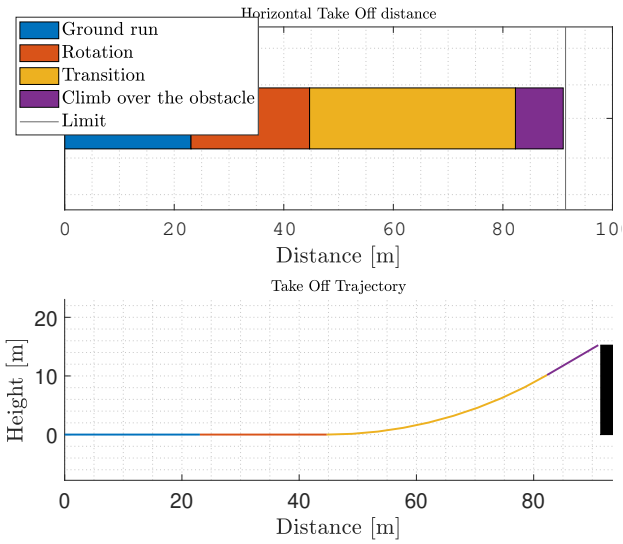

Figure 45: Take Off run.

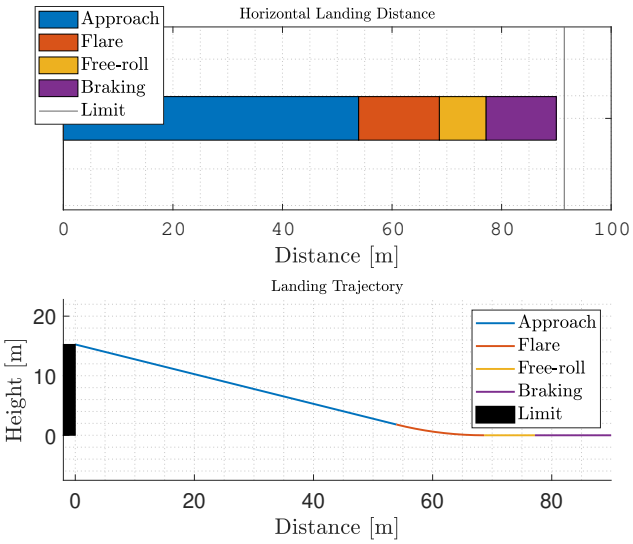

Figure 46: Landing run.

11.2 Integral Performances

11.2.1 Range

In Fig. 47 it's possible to see the variation of range as a function of the payload onboard.

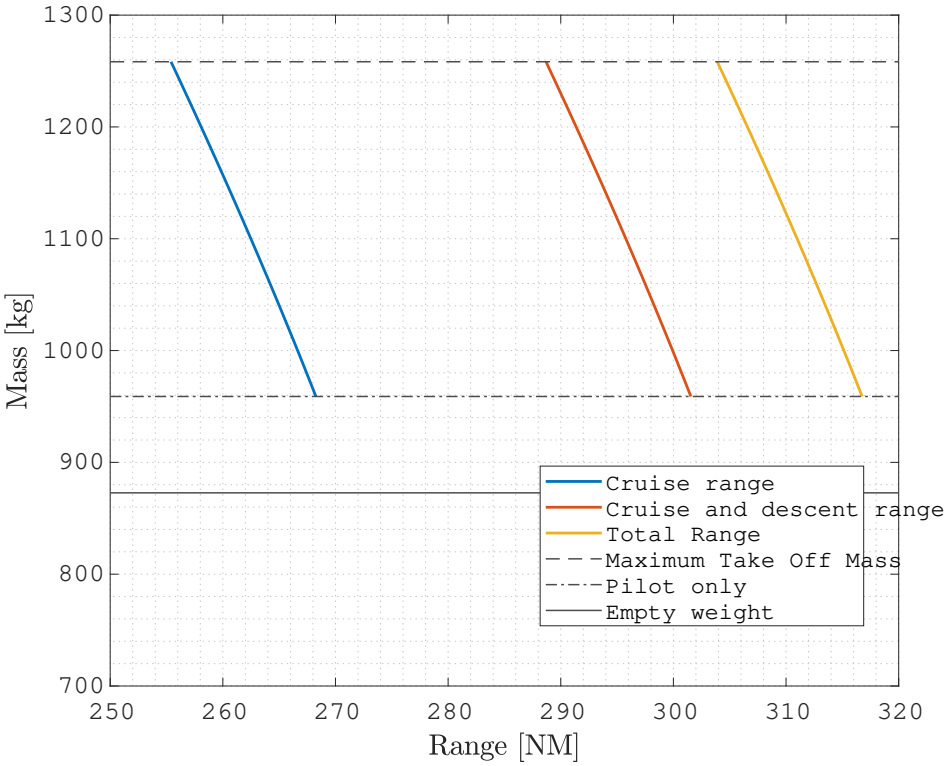

Figure 47: Payload chart.

These ranges are computed considering a cruise altitude of 10000 ft and a speed of 170 KTAS.The maximum range obtained is 316 NM, with only the pilot onboard.
It's important to notice that the computed ranges don't include the additional range required to reach the alternate airport nor the one granted by the IFR reserves.
In case of an in-flight loss of the ICE, a range of 40 NM is granted by the energy reserves in the batteries.

11.2.2 Endurance

Maximum endurance can be obtained flying at 77 KTAS, the speed with the maximum value of the power index F, Eq. (14), in cruise condition. This speed is also equal to the speed with

minimum P_r. The resulting endurance is equal to 90 min with a full payload.

$$F = \frac{L}{D}\sqrt{C_L} \tag{14}$$

11.2.3 Climb and descent times

Simulating a typical mission, the time required to reach cruise condition from take off results equal to 12 min in MTOW conditions. It's important to note that the climb is composed of two phases:

1. An initial climb with vertical speed of 1500 fpm up to 1500 ft;
2. A following climb with vertical speed of 750 fpm up to cruising. altitude

With a similar procedure, the descent time from cruise conditions to ground has been obtained imposing a vertical speed of -500 fpm and results in 20 min.

11.3 Instantaneous performances

11.3.1 Drag and Power curves

Fig.48 shows the required power (P_r) and the available power (P_a) as function of speed in MTOW and cruise conditions. Particularly, P_a is obtained from $P_{EM,n}$ with a reduction caused by propeller efficiency. As an initial approximation, P_a has been considered constant with speed so that the available thrust (Eq.15) is defined as:

$$T = \frac{P_a}{V} \tag{15}$$

This approximation isn't appropriate at low speeds given that it leads to an overestimation of the available thrust. However, in this case, it has been considered a reasonable choice when coupled with the knowledge of the minimum stall speed.
The behaviour of trust and drag with speed is shown in Fig.49.

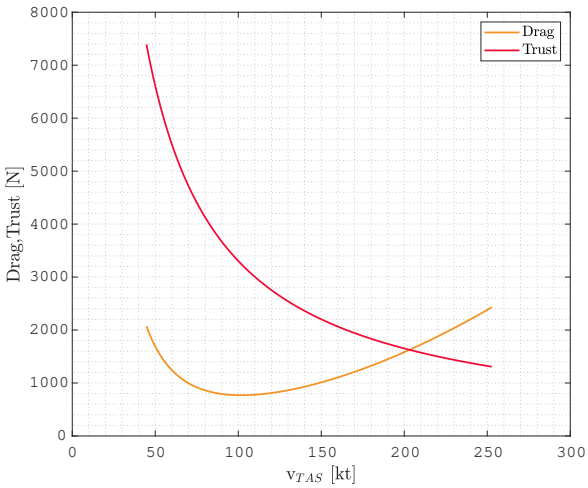

Figure 48: P_a and P_r as a function of speed.

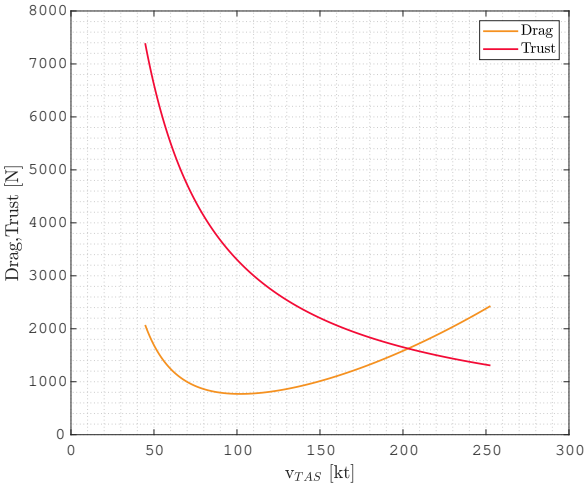

Figure 49: Trust and Drag as a function of speed.

11.4 Vertical speed

The maximum vertical speed as function of speed is obtained by evaluating the Specific Excess Power (SEP) available (Eq.16), computed as:

$$SEP = V_v = \frac{P_a - P_r}{W} \tag{16}$$

The resulting vertical speed is shown in Fig.50.

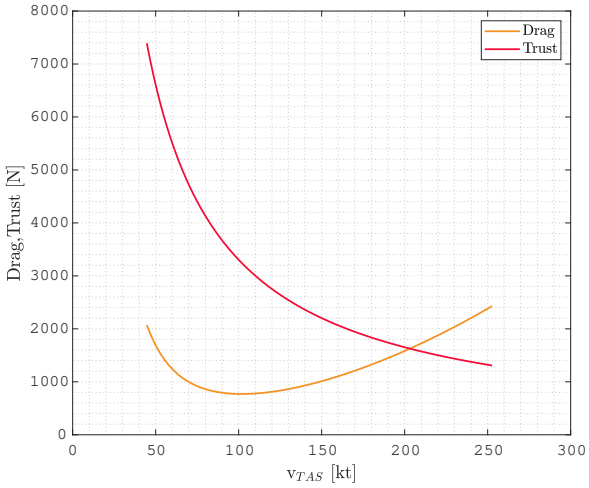

Figure 50: Vertical speed with respect to speed.

11.4.1 Climb angle

In a similar way, the climb angle (Eq.51) can be computed dividing the SEP by speed:

$$sin\gamma = \frac{T - D}{W} \tag{17}$$

Results are shown in Fig.51.

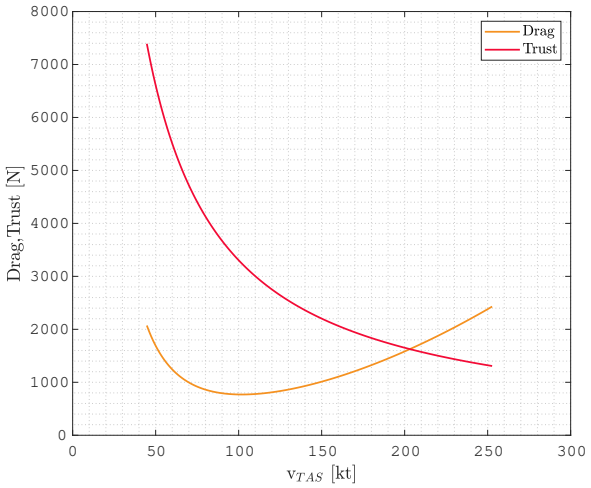

Figure 51: Climb angle with respect to speed.

11.4.2 Turn performance

In order to study performances during a corrected turn, the following conditions must be taken into account:

1. limitation on the load factor caused by stalling speed;
2. structural limit;
3. available trust.

Results for each limitation are shown in the graphs in Fig.52. Particularly, it's possible to note that the structural limitation on the load factor do not limit performances.

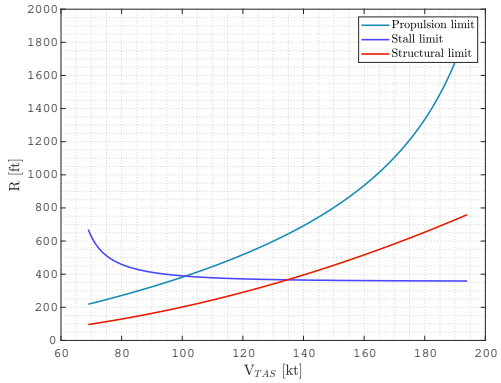

(a) Turn radius.

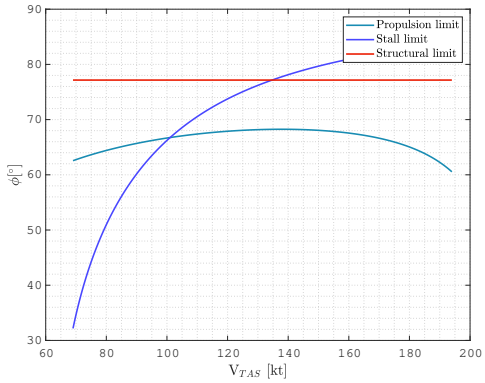

(b) Bank angle.

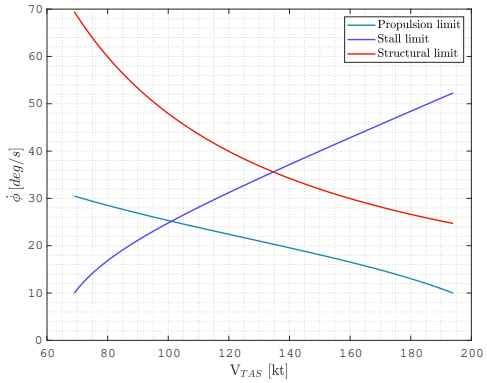

(c) Turn rate.

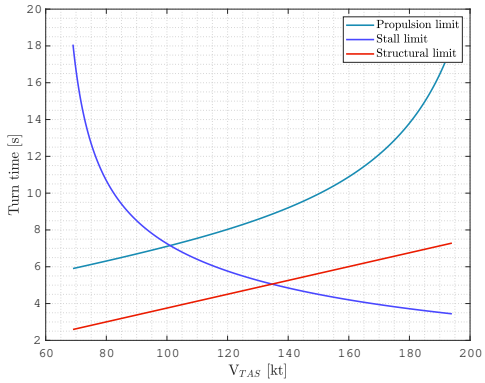

(d) Turn time.

Figure 52: Turn performances.

11.5 Flight envelope

In order to obtain the flight envelope (Fig.53), as a first approximation, the service ceiling has been imposed at 15,000 ft since there's no effect of altitude on available power.

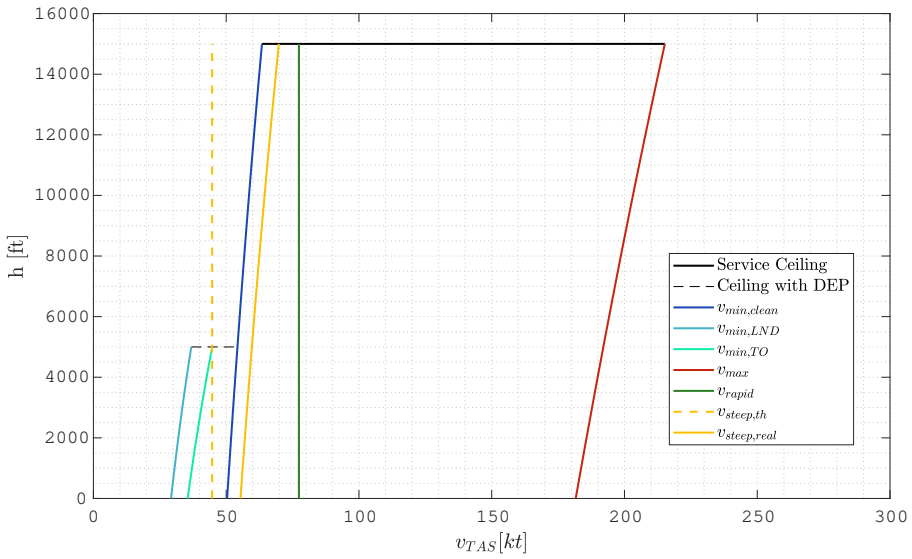

Figure 53: Fligh envelope.

Still considering Fig.53, it is possible to appreciate steep ascent and rapid ascent speeds, respectively computed as the speed in correspondence of the maximum value of γ and vertical velocity, as functions of altitude.

The obtained value for the steep ascent speed results lower than the minimum flight speed in clean configuration. For this reason, the steep ascent speed has been imposed equal to $v_{steep} = 1.1 \cdot v_{min,clean}$.

Up to 5,000 ft the DEP system can be used, lowering the minimum speed. In particular, the take-off configuration grants a $C_L = 4$ with 20° of flaps deflection while the landing configuration grants a $C_L = 6$ with a flap deflection of 30°.

11.6 Mission Simulation

In order to assess the overall capability of the aircraft, a number of simulations were carried out. Once verified HExi's ability to perform the sizing mission, a further test was carried out based on a different mission profile. More specifically, a series of nine legs of 50 nmi each involving take off, cruise and descent was imposed, adding a final loiter phase.

12 Cost analysis

12.1 Introduction

Production and operating costs are estimated based on Eastlake and Blackwell model, already modified by Gudmundsson for a GA aircraft [28]. However, Gudmundsson formulas needed some additional modifications to account for more complicated manufacturing technologies (such as tapered wings or pressurization) and the use of a hybrid-electric propulsion [30]. In particular, the degree of hybridization p_{hyb} (Eq.18) is defined as the power ratings of the electric motor $P_{EM,n}$ and the thermal motor $P_{ICE,n}$ depending on the required total system power $P_{Total,n} = P_{EM,n} + P_{ICE,n}$:

$$p_{hyb} = \frac{P_{EM,n}}{P_{Total,n}} \tag{18}$$

In addition, another important modification that must be taken into account is the application of the "learning curve" so that the cost is adjusted thanks to the Quantity Discount Factor (F_{QDF}, see Eq.19). This factor depends on the quantity of units produced (N) and the application of an experience effectiveness adjustment factor (F_{exp}) that accounts for the increasing productivity of technicians with increasing experience. More precisely, $F_{exp} = 95\%$ considering the innovation of the project [30].

$$F_{QDF} = F_{exp}^{1.4427ln(N)} \tag{19}$$

Moreover, given that Gudmundsson formulas [28] are related to the year 2012, it was necessary to update the value of CPI to take into account the inflation until 2031. CPI Data are available from the website of Bureau of Labor Statistics up to year 2021 [31]. Then, in order to estimate CPI from 2021 to 2031, predictions based on a study of the Minnesota Department of Education [32] were considered. Finally, a MATLAB code named *cost analysis* has been developed and results are reported in the next paragraphs.

12.2 Production Costs

In order to estimate production costs (reported in Table 28), the strategy followed was breaking them down into the major contributions of:

- Total cost of engineering for the aircraft (C_{ENG}), estimated based on engineering hours that includes operations such as airframe design and analysis, test engineering and configuration control;
- Development support costs (C_{DEV}), that consists in operations required to support development effort such as administration, logistics, etc.;
- Flight Test Operations (C_{FT}), covering costs for completing certifications;
- Tooling (C_{Tool}), estimated based on tooling hours necessary for designing, fabricating and maintaining required tools;
- Manufacturing Labor (C_{MFG}), estimated based on the number of man-hours to fabricate the aircraft;
- Quality Control (C_{QC});
- Total Material Cost (C_{MAT}) for raw materials;

Additional costs for avionics (C_{av}), DEP (C_{DEP}) and ICE (C_{ICE}) are considered and obtained from manufacturer websites [33],[34],[35]. In absence of further informations, costs for the electric motor (C_{EM}, same as the one for the generator) and batteries (C_{BAT}) are estimated from reference values in the literature ([36],[30]). It is important to note that some assumptions have been made in order to set necessary input values to compute previous costs:

- 360 units (N) are going to be produced in 5 years with a production rate of [4,5,5,6,10] units/month from 2029 to 2034. Production is assumed to start in 2029 in order to wait for new technologies and also to be able to enter into service in 2031 with 156 aircraft to be split between Texas and California. These two States are chosen because of the availability of minor airports (section 3) that could allow a fast diffusion of the service and the possibility to test its efficiency. In the following years, with the increasing quantity of available units, HExi will be operating all over the USA;
- two prototypes are constructed;
- the aircraft is considered to be made 100% with composite materials;

- the production site is placed in the USA and so, rates for engineering, tooling and manufacturing are taken as average quantities in the USA estimated for 2029.

	Type of Cost	**Value**
Fixed Cost	C_{ENG}	$41,080,231.71$
	C_{DEV}	$5,269,651.13$
	C_{FT}	$235,889.18$
	C_{Tool}	$106,840,198.61$
Variable Cost	C_{MFG}	$56,016,910.15$
	C_{QC}	$11,175,373.57$
	C_{MAT}	$12,808,906.93$
	C_{av}	$41,735$
	C_{ICE}	$48,000$
	C_{DEP}	$13,740$
	C_{EM}	$31,800$
	C_{BAT}	$3,069.10$
Total Cost	$233,565,505.37$	
Cost per Unit	$648,793.07$	
Price per Unit	$778,551.68$	

Table 28: Production Costs for N = 360 at the end of 2034

As it is possible to note from Fig. 54, costs decrease with increasing quantity of aircraft produced so that, in 5 years, it will be possible to obtain a unit cost equal to $778,551.68$ (Table28).

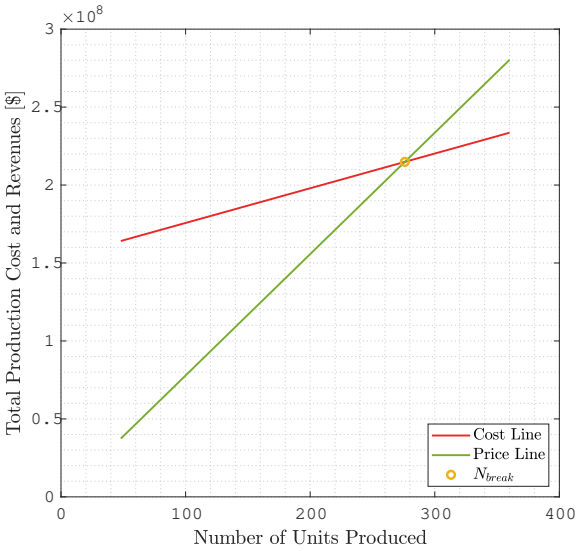

Figure 54: Production cost.

12.3 Operating Costs

Operating costs must be computed to evaluate the cost of the ownership of the aircraft per hour flown. In order to evaluate operating costs, it's necessary to make some additional assumptions beyond previous modifications at Gudmundsson formulas [28]:

- the number of flight hours per year (Q_{FLGT}) has been estimated considering 4 flight per day with missions of 200 min;
- Maintenance to flight hour ratio (F_{MF}) is calculated considering 0.3 maintenance man-hours required per flight hour and adjusted for characteristics that mostly affect maintenance effort (easy engine acces, etc.);
- Navigation fees are charged from ATM operators in relationship with the range flown so that $k_{NAV} = 892.5000\$/km$ [30];

Also for operating costs, exactly as for production cost, the strategy of breaking them down into the following major contributions was adopted (Table29):

- Maintenance Cost (C_{AP});
- Storage Cost (C_{STOR}), considering a cost of storage of $1500\$/year$ for an increasing number of hangar. In particular, an hangar is considered to host five aircraft so that $N_{hangar} = [10, 22, 34, 48, 72]$ with increasing number of available aircraft;
- Crew Costs (C_{Crew}), only pilot;
- Annual Insurance Cost (C_{ins});
- Annual Inspection Cost (C_{insp});
- Engine Overhaul Fund (C_{over}), estimated with an overhaul time of 1200hr and an average cost of the overhaul of 10000\$;
- Annual Fuel Cost (C_{fuel}), considering the characteristics of AVIGAS100LL;
- Annual Energy Cost (C_{energy}), considering the characteristics of the batteries;

- Cost for Airport and ATM fees (C_{FEES}), as a result of landing, ground operation and navigation fees.

Type of Cost	Value
C_{AP}	$20,498,400.00$
C_{STOR}	$1,296,000$
C_{Crew}	$87,600,000$
C_{ins}	$12,178.28$
C_{insp}	500
C_{over}	$23,415,275.30$
C_{fuel}	$25,875,692.31$
C_{energy}	$17,080,083.11$
C_{FEES}	$379,551.85$
Total Yearly Cost	$176,157,680.84$
Total Yearly Cost per Aircraft	$489,326.89$
Cost Flight per Hour	100.55

Table 29: Operating Cost for N = 360 at the end of 2034.

As it is possible to note from Fig.55a and Fig. 55b, both the total yearly operating cost and the cost per flight hour decrease with increasing number of aircraft in service (and so with an increasing number of flight hours).

Product price is assumed to be 30% more than its cost [30].

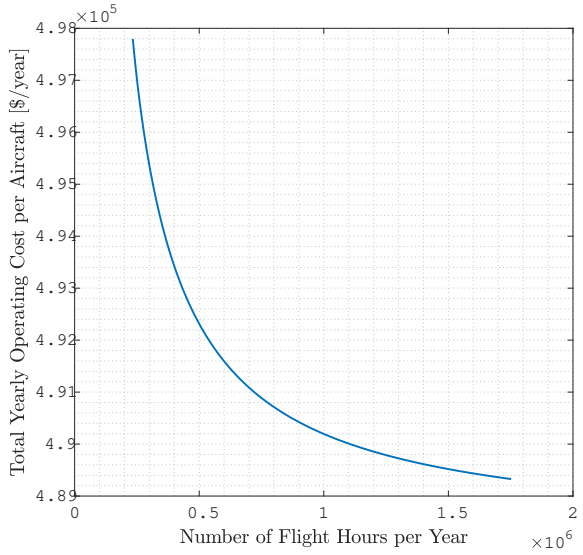

(a) Single Unit Cost.

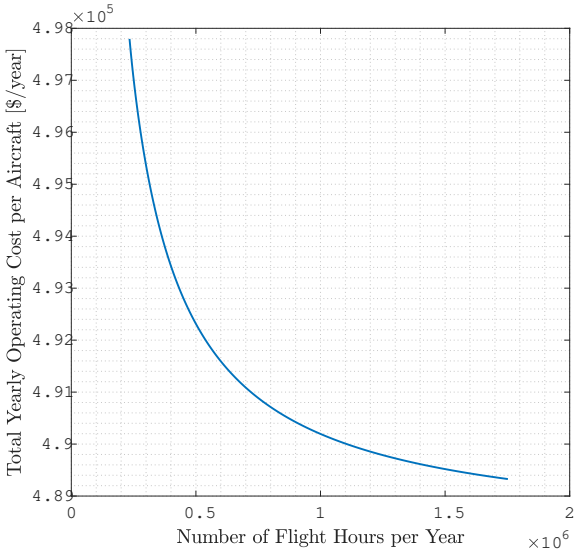

(b) Cost Flight per Hour.

12.4 Break Even Analysis

Break-even analysis determines how many units must be produced before revenue equals the cost incurred. Particularly:

$$N_{break,1} = \frac{total\ fixed\ cost}{price\ per\ unit - unit\ variable\ cost} \tag{20}$$

considering that the aircraft will be sold with a percentage of 20% profit ("Price per Unit" in Table 28). As a result, (Fig.56), $N_{break} = 276$

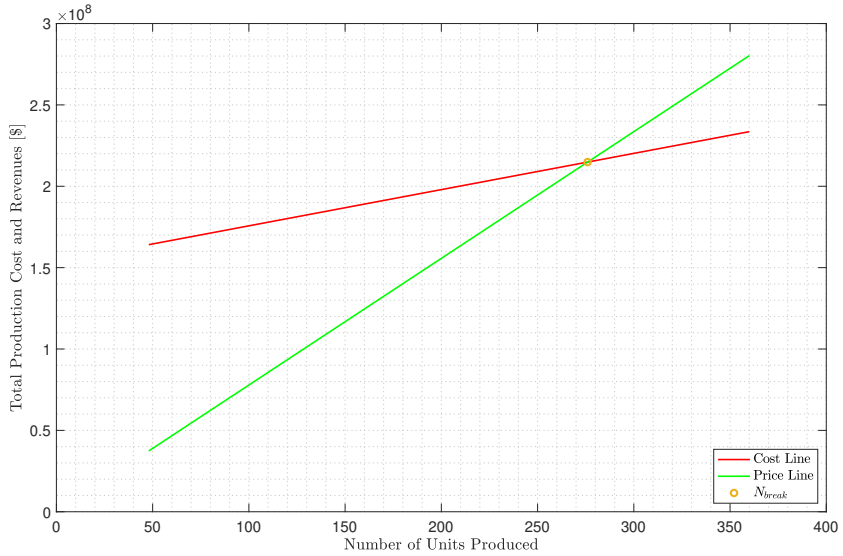

Figure 56: Break Even Point.

A second scenario was studied considering that the aircraft won't be sold and the service will be distributed autonomously.

In this case, revenues will be represented by the tickets sold to fly with HExi. For this reason, the distance rate (Eq.21) to fix the price of the tickets including 20% profit is calculated as follows:

$$Dist_{Rate} = \frac{(Cost\ per\ Unit + Total\ Yearly\ Cost\ per\ Aircraft \cdot Aircraft\ Life) \cdot 1.2}{N_{payload} \cdot d_{range} \cdot N_{flight} \cdot Aircraft\ Life} \tag{21}$$

where $Aircraft\ Life$ is assumed to be equal to 15 years. As a result $Dist_{Rate} = 0.26\$/km$, making HExi competitive with ground transportation and also respecting one of the main objectives of this project, which is keeping low costs. Both sales strategies results to be valid.

As an example, before reaching the break-even point and before entering into service, it could be possible to sell some units in order to start gaining revenues to cover production costs. Successively, when a wider diffusion of HExi service is reached, all units could be employed to only distribute the service autonomously.

13 Safety and Maintenance

13.1 Certification and safety

Based on the size of HExi, its design followed FAA Part 23 certification, as required. In particular, due to the fact that the DEP system is not designed for propulsive goals, the aircraft can be categorized as a single engine.

It is important to observe that, because of the non-conventional design, some of the aircraft components require a review or an adaption of the certification requirements, in order to meet all the standards for successfully completing the certification process.

More in details, the propulsion system -more precisely, the electric aspects - requires a particular attention, both in terms of regulations and safety.

Indeed, related to the latter aspect, the risk assessment has been conducted on the basis of the guidelines provided by the International Civil Aviation Organization (ICAO) and reported in Fig.57.

Risk probability	**Risk severity**				
	Catastrophic A	Hazardous B	Major C	Minor D	Negligible E
Frequent 5	5 A	5 B	5 C	5 D	5 E
Occasional 4	4 A	4 B	4 C	4 D	4 E
Remot 3	3 A	3 B	3 C	3 D	3 E
Improbable 2	2 A	2 B	2 C	2 D	2 E
Extremely improbable 1	1 A	1 B	1 C	1 D	1 E

Figure 57: ICAO risk matrix.

The resulted risk matrix is presented in Fig.58.

Project hazard summary	Probability/severity classification	Risk mitigation	Compliance
Bird strike	3 B	Anti-bird strike system	2 C
Ice formation	4 B	Anti-ice system	1 B
Mid air collision	3 A	TCAS and ATC	1 A
1 EM inoperative	3 C	PMAD	3 D
12 EM inoperative	1 A	PMAD	1 B
6 EM inoperative	2 B	PMAD	2 C
Nose EM inoperative	3 A	PMAD	3 B
Thermal engine / generator failure	2 B	PMAD	2 D
Cockpit air contamination	3 A	Oxygen system	3 B

Figure 58: Effect of mitigation on risk and compliance.

In addition, because of the integration of a fly-by-wire system to govern the aircraft operations, also both the software and hardware parts need a certain attention in terms of their specific certification and safety requirements.

13.2 Maintenance

In order to guarantee aircraft safety, keep the aircraft in service and maximise value of asset (airframe, engines and components), the following kind of maintenance effort must be taken into account:

- Line Maintenance such as pre-flight checks, daily checks and component replacement or minor repairs and modifications. When designing the internal layout (section 10), particular attention has been given to guarantee an easy access to relevant components (Fig.59, Fig.60);

- Heavy Maintenance such as checks for deterioration of the airframe, engines and systems. In order to ease these kind of operations, beyond an easy access to relevant components, specialised staff is employed. For this aim, 0.3 maintenance man-hours required per flight hour and an overhaul time of 1200hr have been assumed (section 12).

Fig.59 and Fig.60 show the access points to the following components for maintenance operations:

- two cowlings are considered to access EM and ICE and they are respectively placed one in the front and the other one in the back of the aircraft (Fig.59);
- the lower part of the fuselage can be extracted in order to get access to batteries. Particularly, two battery slots are foreseen in order to guarantee an easier access (Fig.60)

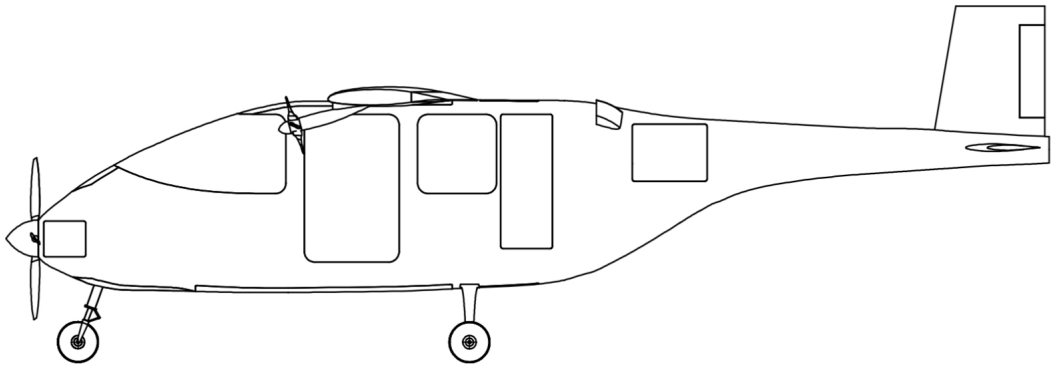

Figure 59: Lateral View.

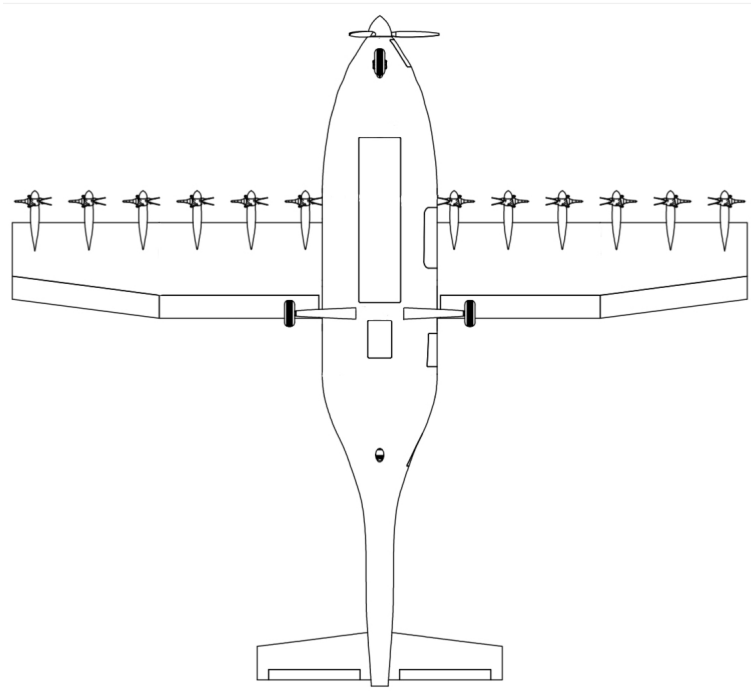

Figure 60: Bottom View.

14 Conclusions

Speed, Comfort and Sustainability are three perfect words to describe HExi, a hybrid electric STOL aircraft meant to serve the Urban Air-Mobility market all over the USA.
Speed is achieved thanks to:

- the possibility of travelling a maximum range of 300 NM in 2h 35min with a target velocity of 170 KTAS making HExi competitive with the transportation at ground as well with already existing similar aircraft.

Comfort is conceived in a way never seen before:

- the implementation of the blown technology through a DEP system makes possible taking off and landing in very short distances. This allows the possibility of completing missions with multiple TO and LND in order to distribute a real Taxi Service;
- thanks to the landing gear setup and the low tires inflation pressure, HExi can land on different type of surfaces. In this way, it will be possible to reach outskirts or badly connected cities reducing as much as possible the typical disadvantages of ground transportation.

Sustainability is one of the major strenghts of HExi:

- thanks to full electric TO and LND phases, it is possible to obtain a level of CO_2 emissions equal to $34 pas \cdot /km$ making the aircraft extremely competitive with current modes of transportation.

It is also important to underline that thanks to the use of composites materials for the structure, it was possible to draw the shape of the fuselage with excellent aerodynamic performances and with an eye catching design. Moreover, it must not be forgotten that flying with HExi will cost only 0.26 $\$/km$ and so, in addition to all previous advantages, it will be competitive from the economic point of view.
A perfect combination of innovative technologies, performance advantages, low emissions and economical benefits make HExi the revolution of UAM market and the forerunner for the distribution of the air-taxi service on a large scale.

[*]

References

[1] URL: https://www.airnow.gov/.

[2] URL: https://www.americashealthrankings.org/explore/annual/measure/air/state/ALL.

[3] URL: https://health.gov/healthypeople.

[4] Akira Nishizawa Hiroshi Kobayashi. *Decrease in Ground-Run Distance of Airplanes by applying electrically driven wheels*. Tech. rep. Japan Aerospace Exploration Agency, 2010.

[5] Dr. Jan Roskam. *Airplane Design*. Design, Analysis and Research Corporation, 1997.

[6] Daniel P. Raymer. *Aircraft Design - A Conceptual Approach - Sixth Edition*. AIAA Education Series, 2018.

[7] Andrea Matrone. "Performance-Based Preliminary Sizing of Aircraft with Distributing Propulsion". MA thesis. Politecnico di Milano, 2019-2020.

[8] M.Galea V.Madonna P.Giangrande. *Electrical Power Generation in Aircraft: review, challenges and opportunities*. Tech. rep.

[9] URL: https://warteraviation.com/de/fuels/avgas-100-ll/.

[10] URL: https://www.cei.washington.edu/education/science-of-solar/battery-technology/#:~:text=They%20have%20one%20of%20the,%2DCd%20or%20Ni%2DMH.

[11] Weisheng Cui Renheng Wang. *Lithium metal anodes: Present and future*. Tech. rep. School of Metallurgy, Environment, Central South University - College of Physics, and Optoelectronic Engineering, Shenzhen University, 2020.

[12] URL: https://www.frontiersin.org/articles/10.3389/fenrg.2019.00123/full.

[13] URL: https://ucsdnews.ucsd.edu/pressrelease/meng_science_2021#:~:text=Silicon%20anodes%20are%20famous%20for,today's%20commercial%20lithium%20ion%20batteries..

[14] Dr.Ajay Misra. *Summary of 2017 NASA Workshop on Assessment of Advanced Battery Technologies for Aerospace Applications*. Tech. rep. NASA Glenn Research Center, 2018.

[15] Carlo E.D. Riboldi. *An optimal approach to the preliminary design of small hybrid-electric aircraft*. Tech. rep. Politecnico di Milano, 2018.

[16] Mohammad H. Sadraey. *Aircraft Design - A Systems Engineering Approach*. WILEY, 2013.

[17] Ravinder Kumar R.D.Jilte. *Numerical Investigation on Cooling Performance of Li-ion battery thermal management system at high galvanostatic discharge*. Tech. rep.

[18] URL: https://ulpower.com/en/engines/ul520/ul520t.

[19] URL: https://www.h3x.tech.

[20] Daniele Imo. "Optimal Approach to the Preliminary Design of Aircraft Propellers with Regeneration Capability". MA thesis. Politecnico di Milano, 2021-2022.

[21] Michael D.Patters. *Conceptual Design of High-Lift Propeller Systems for Small Electric Aircraft*. Tech. rep. Georgia Institute of Technology, 2016.

[22] Joseph M. Derlaga Brandon L. Litherland Michael D. Patterson and Nicholas K. Borer. *A Method for Designing Conforming Folding Propellers*. Tech. rep. NASA Langley Research Center.

[23] URL: https://neumotors.com/brushless-motor-manufacturing/neumotors-4400-series-bldc-motors-1000-to-4000-watt-class/.

[24] URL: https://www.transit.dot.gov/sites/fta.dot.gov/files/docs/PublicTransportationsF pdf.

[25] *50 Steps Toward Carbon-Free Transportation Rethinking U.S. Transportation Policy to Fight Global Warming*. Tech. rep. U.S. Public Interest Research Group,Frontier Group.

[26] ALBERT E. von DOENHOFF IRA H.ABBOTT and LOUIS S. STIVERS Jr. *Summary of Airfoil Data*. Tech. rep. National Advisory Committee for Aeronautics, 1945.

[27] URL: http://airfoiltools.com/.

[28] Snorri Gudmundsson. *General Aviation Aircraft Design*. Butterworth-Heinemann, 2014.

[29] URL: http://www.ecfr.gov/cgi-bin/text-idx?tpl=/ecfrbrowse/Title14/14cfr23_main_02.tpl.

[30] Raouf IBRAHIM. "Market and Cost Analysis of Hybrid-Electric Aircraft". MA thesis. Politecnico di Milano, 2017-2018.

[31] URL: https://www.bls.gov/.

[32] URL: ps://education.mn.gov/MDE/index.html.

[33] URL: https://www.garmin.com/en-US/c/aviation/general/flight-decks-displays/.

[34] URL: https://neumotors.com/brushless-motor-manufacturing/neumotors-4400-series-bldc-motors-1000-to-4000-watt-class/.

[35] URL: https://ulpower.com/en/engines/ul520/ul520t.

[36] URL: https://www.team-blacksheep.com/products/prod:apd_200f3_x_14s.

[37] URL: https://skybrary.aero/articles/maintenance-programme.

[38] John D.jr Anderson. *Introduction to Flight*. McGraw-Hill Education, 2016.

[39] URL: https://www.caranddriver.com/news/a38711469/toyota-solid-state-batteries-2025/.

[40] URL: https://www.frontiersin.org/articles/10.3389/fenrg.2019.00123/full.

List of tools used:

- MATLAB, url: https://it.mathworks.com/products/matlab.html
- OpenVSP, url: http://openvsp.org/
- XFLR5, url: http://www.xflr5.tech/xflr5.htm
- JavaProp, url: https://www.mh-aerotools.de/airfoils/javaprop.htm
- SolidWorks, url: https://www.solidworks.com/